TIGHT BINDING INVESTIGATION OF GRAPHENE NANOSTRUCTURES UNDER MAGNETIC FIELD

A THESIS SUBMITTED TO
THE GRADUATE SCHOOL OF NATURAL AND APPLIED SCIENCES
OF
MIDDLE EAST TECHNICAL UNIVERSITY

BY

FIRAT YALÇIN

IN PARTIAL FULFILLMENT OF THE REQUIREMENTS
FOR
THE DEGREE OF MASTER OF SCIENCE
IN
PHYSICS

JANUARY 2019

Approval of the thesis:

TIGHT BINDING INVESTIGATION OF GRAPHENE NANOSTRUCTURES UNDER MAGNETIC FIELD

submitted by **FIRAT YALÇIN** in partial fulfillment of the requirements for the degree of **Master of Science in Physics Department, Middle East Technical University** by,

Prof. Dr. Halil Kalıpçılar
Dean, Graduate School of **Natural and Applied Sciences** ________________

Prof. Dr. Altuğ Özpineci
Head of Department, **Physics** ________________

Assoc. Prof. Dr. Hande Toffoli
Supervisor, **Physics, METU** ________________

Examining Committee Members:

Prof. Dr. Oğuz Gülseren
Physics, Bilkent University ________________

Assoc. Prof. Dr. Hande Toffoli
Physics, METU ________________

Prof. Dr. Ahmet Oral
Physics, METU ________________

Date: 31.01.2019

I hereby declare that all information in this document has been obtained and presented in accordance with academic rules and ethical conduct. I also declare that, as required by these rules and conduct, I have fully cited and referenced all material and results that are not original to this work.

Name, Surname: Fırat Yalçın

Signature :

ABSTRACT

TIGHT BINDING INVESTIGATION OF GRAPHENE NANOSTRUCTURES UNDER MAGNETIC FIELD

Yalçın, Fırat
M.S., Department of Physics
Supervisor: Assoc. Prof. Dr. Hande Toffoli

January 2019, 50 pages

Electrons moving under the effects of a two dimensional periodic potential and a magnetic field perpendicular to this two dimensional plane has been the focus of many different studies for a long time. The interplay between the two length scales in this problem, lattice constant and the characteristic magnetic length, results in interesting phenomena such as the Hofstadter's butterfly. The bulk of the studies done so far has focused on uniform magnetic fields. The only requirement for the vector potential is that its closed loop integral resulting in the correct flux piercing through the loop. This allows us to use a rather unconventional gauge where we set certain values for the line integrals instead of solving the line integrals with a known vector potential. Using this gauge, we can study the effects of inhomogeneous fields in a very efficient way. The electronic structures of hexagonal flakes, Y-shaped junctions and cross-shaped junctions of different sizes have been studied using tight-binding method and the optimal gauge. The results show emergence of new states around the Fermi level localized on the lattice sites where the magnetic fields are applied.

Keywords: graphene, tight-binding, magnetic field, nanostructure, inhomogeneous magnetic field, density of states, local density of states, junction

ÖZ

GRAFEN NANOYAPILARIN MANYETİK ALAN ALTINDA SIKI-BAĞLANIM İNCELEMESİ

Yalçın, Fırat
Yüksek Lisans, Fizik Bölümü
Tez Yöneticisi: Doç. Dr. Hande Toffoli

Ocak 2019 , 50 sayfa

İki boyutlu bir periyodik potansiyel ve bu iki boyuta dik bir manyetik alanın etkisi altındaki elektronlar uzun yıllardır birçok farklı araştırmaya konu olmuştur. Örgü sabiti ve karakteristik manyetik uzunluk ölçeklerinin etkileşimi, Hofstadter kelebeği gibi ilginç olaylara yol açmaktadır. Yapılan çalışmaların büyük bölümü sabit manyetik alanlar üzerine yoğunlaşmıştır. Vektör potansiyelin sağlaması gereken tek şart, bu potansiyelin kapalı döngü integralinin döngüden geçen manyetik akıya eşit olmasıdır. Bu, bilinen bir vektör potansiyel kullanaral çizgi integralleri hesaplamak yerine, bu integrallerin değerlerini tanımlamamızı sağlayan bir ölçü kullanabilmemizi sağlar. Bu ölçüyü kullanarak homojen olmayan manyetik alanları oldukça etkili bir şekilde çalışabiliriz. Bu çalışmada farklı büyüklüklerde altıgensel pul, Y-şekilli bağlantı ve çapraz-şekilli bağlantıların elektronik yapılarını inceliyoruz. Sonuçlar Fermi seviyesi üzerinde manyetik alanın uygulandığı konumlarda lokalize yeni durumların ortaya çıktığını göstermektedir.

Anahtar Kelimeler: grafen, sıkı-bağlanım, manyetik alan, nanoyapılar, homojen olmayan manyetik alan, durum yoğunluğu, yerel durum yoğunluğu, bağlantı

To my family

ACKNOWLEDGMENTS

This thesis would not be possible without the help of others and I would like to thank them deeply.

Foremost, I would like to thank my advisor Assoc. Prof. Dr. Hande Toffoli for her constant support and encouragement. In a way, she was both my advisor and counselor. When I was feeling down and hopeless, she would always find a way to show me that things are actually not so bleak and always tried to cheer me up.

Many thanks go to my father, who always believed in me and whom I imagine would be the happiest person if he saw how I turned things around. My mother, for unconditional support through all my life, and constantly worrying that I skip breakfasts in the morning. I feel so lucky to have such a great family and I will always feel deeply grateful for them.

I would like to thank Nevra Akalın, who holds a special place in my heart. She always supported me and warmed my heart with her love, and she was always there for me whenever I needed it.

I am especially thankful to my dear friends Şahin Kürekçi and Gözdenur Toraman. They are the reason I look forward to my lunch breaks and the conversations we have always bring joy to my day.

Many thanks go to my colleagues, Merve Baksi, Elif Sert and, Duygu Gizem Şentürk for the discussions we had, be it about physics or life in general.

Special thanks go to my almost-three-year old niece, Elif Ece Demir, for being the cutest and the most intelligent little person I know. She always made sure that I take breaks from my studies to play with her whenever she was around.

It goes without saying that I owe so much to all the instructors in my department. I learned so much from them during these last couple of years and this knowledge

is not limited to subjects in physics but extend to how to be a good instructor. This helped me immensely in my teaching assistantship work and I feel lucky to have such role models around me to learn from.

Finally, I would like to thank my family for just being the best and fun to be around, I feel extremely lucky to have such support in my life.

TABLE OF CONTENTS

ABSTRACT v

ÖZ vii

ACKNOWLEDGMENTS x

TABLE OF CONTENTS xi

LIST OF TABLES xiii

LIST OF FIGURES xiv

CHAPTERS

1 INTRODUCTION 1

2 METHOD 5

  2.1 Tight Binding Method without Magnetic Field 5

    2.1.1 Example: Square Lattice with Single Atom Basis 10

    2.1.2 Example: Primitive cell of graphene with only p_z orbitals . . . 12

  2.2 Tight Binding Method Under a Magnetic Field 12

    2.2.1 Example: Square Lattice Under Uniform $\vec{B}$ 14

    2.2.2 The Optimal Gauge 16

    2.2.3 Inhomogeneous Fields 18

3 CALCULATION DETAILS 21

  3.1 The Systems Investigated 21

3.1.1 Neighbor Table 22

3.2 Density of States 22

3.2.1 Projected(Local) Density of States 23

3.2.2 Magnetic Field 24

4 RESULTS 25

4.1 Size Dependence of DOS 25

4.2 Hexagonal Flakes 28

4.3 Y-shaped Junctions 31

4.4 Cross-shaped Junctions 31

4.5 Magnetic Field Dependence of E=0 States 35

4.6 Size Dependence of Fermi Level States 36

5 DISCUSSION AND FUTURE WORK 41

REFERENCES 43

APPENDICES

A PEIERLS SUBSTITUTION 47

B HARPER’S EQUATION 49

LIST OF TABLES

TABLES

LIST OF FIGURES

FIGURES

Figure 1.1 Hexagonal lattice structure - $\vec{\delta_1}$,$\vec{\delta_2}$, and $\vec{\delta_3}$ as nearest neighbor(NN) vectors and $\vec{a_1}$,$\vec{a_2}$ as primitive lattice vectors 1

Figure 1.2 First Brillouin zone of primitive cell of graphene with $\vec{b}$ as the reciprocal lattice vectors(left). Linear dispersion(also called the Dirac cones) at high symmetry points K and K' (right) 3

Figure 2.1 Square lattice with a single atom basis, where a_1 and a_2 are the primitive lattice vectors. 10

Figure 2.2 Square lattice energies plotted on a k_x/k_y grid with $k_x, k_y \in [-2\pi/a, 2\pi/a]$, with ϵ_{1s} taken to be zero. 11

Figure 2.3 Graphene band structure on a k_x/k_y grid formed on the 1^{st} Brillouin zone. 13

Figure 2.4 Magnetic unit cell for square lattice with single atom basis. The primitive cell is enlarged in $\mathbf{a_1}$ direction and this direction is decided by the Landau gauge used in the problem. 15

Figure 2.5 Hofstadter's butterfly for square(left) and hexagonal(right) lattices with $q = 151$. 16

Figure 2.6 Optimal gauge for graphene: only the line integrals over the paths with red arrows are set to be non-zero. Values for the non-zero line integrals are given by the destination hexagon's x-index n. Reprinted from [1] 17

Figure 2.7 (a) A localized magnetic field creates a flux Φ_1 on a single cell. All the line integrals on the hopping paths above this cell are set to Φ_1. (b) Separate magnetic fields can be treated independently. If they are located on the same vertical slice, the line integrals are set to $\Phi_1 + \Phi_2$ above the upper cell, Φ_1 between, and 0 otherwise. 19

Figure 3.1 Three main graphene nanostructures used in this study. Only one edge variants are shown here. 22

Figure 3.2 Mapping lattice points from hexagonal to an equivalent brick lattice. 23

Figure 4.1 DOS of various sized armchair graphene flakes. Number in the top left is the number of atoms. 26

Figure 4.2 DOS of various sized zigzag graphene flakes. Number in the top left is the number of atoms. 27

Figure 4.3 DOS of Y-shaped(A) junctions of varying sizes. Number in the top left is the number of atoms. 27

Figure 4.4 DOS of Y-shaped(Z) junctions of varying sizes. Number in the top left is the number of atoms. 28

Figure 4.5 DOS(top) and PDOS(bottom) of armchair hexagonal flake with 5514 atoms. B-field Gaussian has a peak at (0,0) with magnitude 20T and σ is 20 angstroms. 29

Figure 4.6 DOS(top) and PDOS(bottom) of zigzag hexagonal flake with 5400 atoms. B-field Gaussian has a peak at (0,0) with magnitude 20T and σ is 20 angstroms. 30

Figure 4.7 DOS(top) and PDOS(bottom) of armchair hexagonal flake with 5514 atoms. B-field is uniform with a magnitude of 20T. 30

Figure 4.8 DOS(top) and PDOS(bottom) of zigzag hexagonal flake with 5400 atoms. B-field is uniform with a magnitude of 20T. 31

Figure 4.9 DOS(top) and PDOS(bottom) of Y-shaped(A) junction with 4929 atoms. B-field Gaussian has a peak at (0,0) with magnitude 20T and σ is 20 angstroms. 32

Figure 4.10 DOS(top) and PDOS(bottom) of Y-shaped(A) junction with 4929 atoms. B-field is uniform with a magnitude of 20T. 32

Figure 4.11 DOS(top) and PDOS(bottom) of Y-shaped(Z) junction with 5010 atoms. B-field Gaussian has a peak at (0,0) with magnitude 20T and σ is 20 angstroms. 33

Figure 4.12 DOS(top) and PDOS(bottom) of Y-shaped(Z) junction with 5010 atoms. B-field is uniform with a magnitude of 20T. 33

Figure 4.13 DOS(top) and PDOS(bottom) of cross-shaped junction with 5200 atoms. B-field Gaussian has a peak at (0,0) with magnitude 20T and σ is 20 angstroms. 34

Figure 4.14 DOS(top) and PDOS(bottom) of Y-shaped(Z) junction with 5200 atoms. B-field is uniform with a magnitude of 20T. 34

Figure 4.15 Number of states in interval [-0.5,0.5]eV as a function of σ for various magnetic field strengths on a an armchair hexagonal flake with 1014 atoms(hence orbitals). Here, the total DOS is normalized to the total number of orbitals in the lattice. 35

Figure 4.16 Number of states in interval [-0.5,0.5]eV as a function of σ for various magnetic field strengths on a an zigzag hexagonal flake with 1014 atoms(hence orbitals). Here, the total DOS is normalized to the total number of orbitals in the lattice. 36

Figure 4.17 Number of states in interval [-0.5,0.5]eV as a function of σ for various magnetic field strengths on a Y-junction(A) with 927 atoms(hence orbitals). Here, the total DOS is normalized to the total number of orbitals in the lattice. 37

Figure 4.18 Number of states in interval [-0.5,0.5]eV as a function of σ for various magnetic field strengths on a Y-junction(Z) with 930 atoms(hence orbitals). Here, the total DOS is normalized to the total number of orbitals in the lattice. 37

Figure 4.19 Number of states in interval [-0.5,0.5]eV as a function of number of atoms for various uniform magnetic field strengths on an armchair flake. Here, the total DOS is normalized to the total number of orbitals in the lattice. 38

Figure 4.20 Number of states in interval [-0.5,0.5]eV as a function of number of atoms for various uniform magnetic field strengths on an armchair flake. Here, the total DOS is normalized to the total number of orbitals in the lattice. 39

CHAPTER 1

INTRODUCTION

Carbon is the primary material of all living organisms and the starting point of organic chemistry. Owing to its high bonding flexibility, systems composed of carbon atoms can take on many different structures, with a high range of variance in their physical and electronic properties. One of the important aspects that define these properties is the dimensionality of these carbon structures. Among these allotropes of carbon, graphene - the two-dimensional(2D) allotrope and the main focus of this thesis - is composed of carbon atoms that form a hexagonal(honeycomb)1.1 lattice.

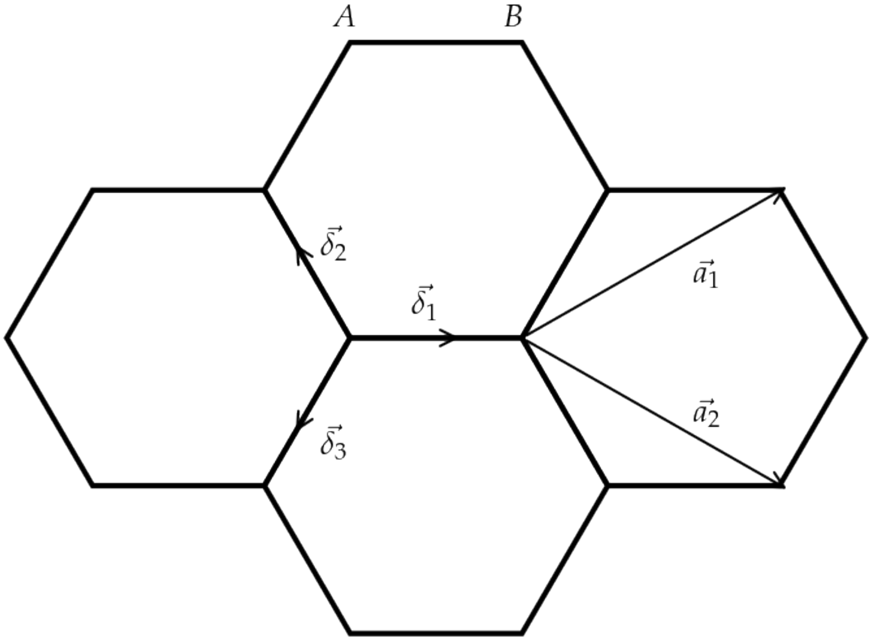

Figure 1.1: Hexagonal lattice structure - $\vec{\delta_1}$,$\vec{\delta_2}$, and $\vec{\delta_3}$ as nearest neighbor(NN) vectors and $\vec{a_1}$,$\vec{a_2}$ as primitive lattice vectors

Graphene plays a crucial role in understanding more complex carbon based structures since it acts as a building block for these structures. For example, fullerene - a zero-dimensional(0D) spherical arrangement of carbon atoms - can be thought of as a rolled up graphene layer where some of the hexagons are distorted into pentagons[2]. The one-dimensional(1D) allotrope, carbon nanotubes(CNTs), are formed by rolling up a graphene sheet in a given direction to form a cylinder, where some of the mechanical and electronic properties vary depending on this direction, also known as the CNTs chirality[3][4]. Last but not least, there is the three-dimensional allotrope known as graphite which is formed by stacking up graphene layers which then interact with each other by weak van der Waals forces[5].

The first theoretical study on the electronic properties of graphene was performed by P.R. Wallace in 1947[6]. In his work, Wallace reported the band structure of graphite using tight-binding approximation and showed that the interactions inside a layer - due to σ-bonds - were much stronger than those between the layers, confirming what we know now as the primary interaction between graphene layers in graphite being van der Waals forces.

For a long time, graphene and other purely 2D materials were considered theoretical toy models and it was assumed that they could never be found in nature. The argument that led to this conclusion was that these types of structures were thermodynamically unstable[7][8]. However, in 2004, Novoselov and Geim[9] managed to exfoliate a single graphene layer from graphite and even though the properties of graphene had been studied by many scientist before them, their work has led to a rapid increase in research on graphene-based systems. For their contribution, they were awarded the Nobel Prize in Physics in 2010.

The structural stability of monolayer graphene is a result of in-plane bonding of carbon atoms. The interaction between two p orbitals and one s orbital results in sp^2 hybridization which leads to a formation of σ-bonds between neighboring carbon atoms[10]. Between three neighbors of a given carbon atom, these bonds form a trigonal bonding structure and this ensures structural stability in all allotropes. The remaining p_z orbitals, which are perpendicular to the monolayer plane, form covalent bonds with the neighbor atoms and form π-bands as a result.

Perhaps the most striking aspect of the electronic properties of graphene is the linear

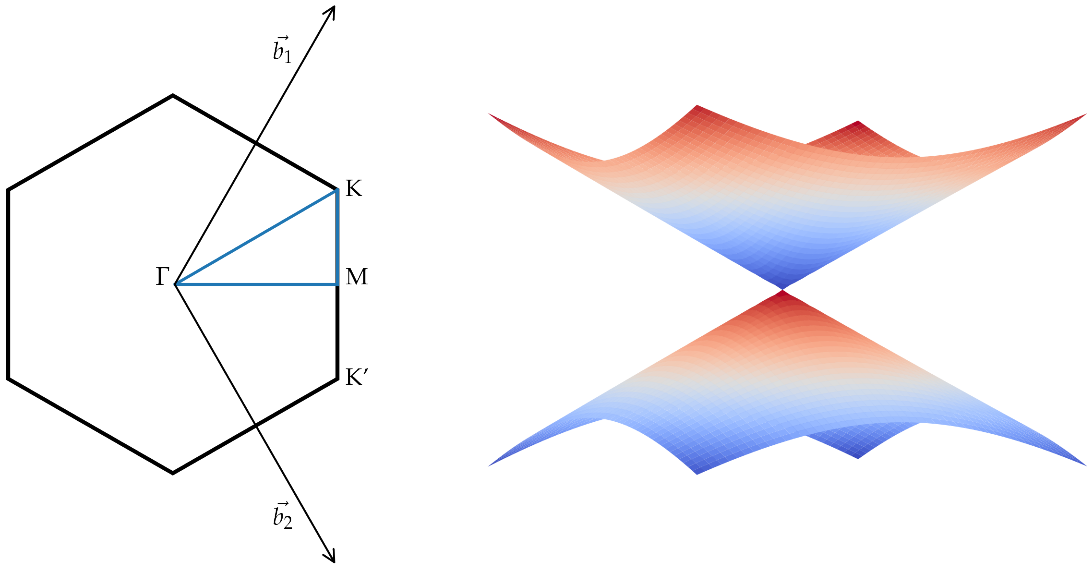

Figure 1.2: First Brillouin zone of primitive cell of graphene with $\vec{b}$ as the reciprocal lattice vectors(left). Linear dispersion(also called the Dirac cones) at high symmetry points K and K' (right)

dispersion relation near high symmetry points $\mathbf{K}$ and $\mathbf{K}'$ in the Brillouin zone1.2[11]. As a result of this, charge carriers near these points act as massless Dirac fermions which move with velocities around 10^6 m/s[12]. This fact allows us to observe and study quantum mechanical effects at much smaller speeds than the speed of light.

Under the effects of magnetic fields, the Dirac fermions exhibit unusual phenomenon compared to regular electrons. One such phenomena is integer quantum Hall effect[13], which was experimentally observed in graphene[14]. The advantage that graphene has here is that these effects are observable even at room temperatures[15]. The high mobility and low density of charge carriers of graphene at near room temperature makes graphene a good candidate for high sensitive Hall sensor devices[16].

On top of these, graphene also has very high thermal conductivity[17] and coupled with its high electronic mobility, it is one of the most promising materials for electronic device applications.

Graphene shows some unexpected mesoscopic effects such as finite conductivity even in the limit of zero temperature and charge carrier density.[18][19]. The presence and types of edges lead to interesting phenomena involving π-electrons[20]. Zigzag and armchair, the most studied types of edges, have substantially different electronic properties. While zigzag edges present localized edge states near the Fermi level, armchair edges do not show such localized states[21][22]. Due to these edge states, ferrimagnetic behavior is observed on zigzag edged nanoribbons[23]. The presence of these localized edge states near the Fermi level leads to a peak in the density of states in zigzag nanoribbons, resulting in metallic behavior, while the armchair nanoribbons have an energy gap that approaches zero as the ribbon width increases[24]. Graphene nanoribbons also show intriguing effects such as Fano-type resonances where conductance is zero for electrons of certain energies[25][26], and nanostructures showing this effect can potentially be used as on/off electronic switches.

Some studies have shown that the electronic levels near the Fermi level of triangular and hexagonal graphene flakes are very close to those of free massless particles in a two-dimensional cavity of the same shape, meaning electrons with these energies flow almost freely on flake surface[27].

In this work, we study the density of states profiles of various zero-dimensional graphene nanostructures with sizes ranging from a couple of atoms to a few thousand using tight-binding method[28]. Tight-binding method is a one-electron method so it completely disregards electron-electron interactions. However, it is still widely employed in the study of electronic structure of solids because it gives good qualitative results in many cases, and can combined with more rigorous theories where it is inaccurate on its own.

This dissertation is divided into three main chapters. First, we will lay down the methodology used without going too much into detail. Some key relations and derivations will instead be presented in the Appendix. Then the systems used and the relevant calculation details will be shortly mentined before going into the results section, where density of states(DOS) and local density of states(LDOS) results will be given. Calculations were done for (i) zero $\mathbf{B}$, (ii) $\mathbf{B}$ in $\hat{k}$ direction with magnitude varying as a Gaussian (iii) uniform $\mathbf{B}$ and the results will be discussed in the final chapter.

CHAPTER 2

METHOD

2.1 Tight Binding Method without Magnetic Field

We start our treatment with the step by step formulation of the tight binding method when no external fields are present and we discuss the effects of an external magnetic field in the upcoming chapters. The tight binding method is frequently used to calculate the electronic band structure of a variety of solids[28]. In this method, the basis functions used to express the crystal wavefunction are generated using highly localized atomic orbitals centered at each lattice site. Since these orbitals are highly localized, they have limited interaction with neighboring lattice sites and the electron is tightly bound to the lattice site it belongs to, hence the name of the method.

The first treatment using the tight binding method was performed by Bloch[29] considering only the s orbitals. Other orbitals were later modeled by Slater and Koster [28]. Although this is a one-electron method, in many cases it gives good qualitative results and can further be combined with other methods to treat cases where the pure tight binding method fails. These cases include but are not limited to correctly describing deep valence states, optical transition energies and correctly describing the properties of heterostructures. Traditionally, the matrix elements in tight binding method, also called the Slater Koster parameters, are fitted to experiment or obtained from more costly ab initio theories[30], making this a very cost effective method for studying the electronic structure of very large systems.

The treatment starts with the statement of Bloch's theorem. The theorem states that the single particle wavefunction of an electron moving in a spatially periodic potential has the form

$$\varphi(\mathbf{k},\mathbf{r}) = e^{i\mathbf{k}.\mathbf{r}}u(\mathbf{r}) \tag{2.1}$$

where $\mathbf{k}$ is a crystal wave vector and $u(\mathbf{r})$ is a periodic function that has the same periodicity as the crystal. One can see that this is essentially a periodic function modulated by a plane wave described by a given wave vector. We can also see that the wavefunction only gains a phase when translated by any Bravais lattice vector

$$\varphi(\mathbf{k},\mathbf{r}+\mathbf{R}) = e^{i\mathbf{k}.\mathbf{R}}\varphi(\mathbf{k},\mathbf{r}) \tag{2.2}$$

which is essentially an equivalent statement to Eq. 2.1.

The discussion here up to the definition of tight-binding parameters will be limited to the case where there is a single atom in the primitive unit cell for the sake of brevity.

We denote an atomic orbital localized on a lattice site $\mathbf{R}$ by $\phi_n(\mathbf{r}-\mathbf{R})$. We next construct Bloch-compliant single-electron state using the sum

$$\varphi_j(\mathbf{k},\mathbf{r}) = \frac{1}{\sqrt{N}}\sum_{\mathbf{R}} e^{i\mathbf{k}.\mathbf{R}}\phi_j(\mathbf{r}-\mathbf{R}) \tag{2.3}$$

where j is the angular momentum of the atomic orbital, the $1/\sqrt{N}$ factor a normalization constant, and the sum is over all the unit cells in the crystal. We can show that this sum obeys the Bloch's theorem by translating it by $\mathbf{R}'$

$$\begin{aligned}
\varphi_j(\mathbf{k},\mathbf{r}+\mathbf{R}') &= \frac{1}{\sqrt{N}}\sum_{\mathbf{R}} e^{i\mathbf{k}.\mathbf{R}}\phi_j(\mathbf{r}-\mathbf{R}+\mathbf{R}') \\
&= \frac{1}{\sqrt{N}}\sum_{\mathbf{R}} e^{i\mathbf{k}.(\mathbf{R}-\mathbf{R}')}e^{i\mathbf{k}.\mathbf{R}'}\phi_j(\mathbf{r}-(\mathbf{R}-\mathbf{R}')) \\
&= \frac{1}{\sqrt{N}}\sum_{\mathbf{R}''} e^{i\mathbf{k}.\mathbf{R}''}e^{i\mathbf{k}.\mathbf{R}'}\phi_j(\mathbf{r}-\mathbf{R}'') \\
&= e^{i\mathbf{k}.\mathbf{R}'}\varphi_j(\mathbf{k},\mathbf{r})
\end{aligned} \tag{2.4}$$

where on the third line, the sum over $\mathbf{R}$ has been transformed to a sum over $\mathbf{R}'' \equiv \mathbf{R}-\mathbf{R}'$, which we can justify since any sum over all the crystal sites is equivalent to one another. For convenience, we will omit the $\mathbf{k}$ dependence from now on, so the reader has to keep in mind that anything defined with these basis functions φ are defined for a specific $\mathbf{k}$. At this point, we can use these functions as a basis set to express the crystal wavefunction. Using Dirac notation

$$\begin{aligned} |\psi\rangle &= \sum_j |\varphi_j\rangle\langle\varphi_j|\psi\rangle \\ &= \sum_j |\varphi_j\rangle C_j \end{aligned} \tag{2.5}$$

where C_j are yet to be determined coefficients. The time-independent Schrödinger equation for the system is given as

$$\hat{H}|\psi\rangle = E|\psi\rangle \tag{2.6}$$

Multiplying from the left by $\langle\psi'|$ and substituting Eq. 2.5 for $|\psi\rangle$, we arrive at an expression for E

$$E = \frac{\sum\limits_{jj'} C^*_{j'} C_j \langle\varphi_{j'}|\hat{H}|\varphi_j\rangle}{\sum\limits_{jj'} C^*_{j'} C_j \langle\varphi_{j'}|\varphi_j\rangle} = \frac{\sum\limits_{jj'} H_{jj'} C^*_{j'} C_j}{\sum\limits_{jj'} S_{jj'} C^*_{j'} C_j} \tag{2.7}$$

Here, $H_{jj'}$ and $S_{jj'}$ can be identified as

$$H_{jj'} = \langle\varphi_{j'}|\hat{H}|\varphi_j\rangle \tag{2.8}$$

$$S_{jj'} = \langle\varphi_{j'}|\varphi_j\rangle \tag{2.9}$$

and they are the elements of transfer and overlap matrices, respectively.

Note that these matrices are defined for a given $\mathbf{k}$ value and have the dimensions $J \times J$ where J is the total number of orbitals contributed by a single atom. At this point, in order to minimize E, we optimize the coefficients $C^*_{j'}$

$$\frac{\partial E}{\partial C^*_{j'}} = \frac{\sum\limits_{j} H_{jj'} C_j}{\sum\limits_{jj'} S_{jj'} C^*_{j'} C_j} - \frac{\sum\limits_{jj'} H_{jj'} C^*_{j'} C_j}{\left[\sum\limits_{jj'} S_{jj'} C^*_{j'} C_j\right]^2} \sum_j S_{jj'} C_j = 0 \tag{2.10}$$

Multiplying by $\sum\limits_{jj'} S_{jj'} C^*_{j'} C_j$ and identifying E from Eq. 2.7, this expression can be simplified as

$$\sum_j H_{jj'} C_j - E \sum_j S_{jj'} C_j = 0 \tag{2.11}$$

Casting this equation into matrix form, we arrive at a generalized eigenvalue equation

$$\big[\widetilde{H} - E\widetilde{S}\big]\vec{C_j} = 0 \tag{2.12}$$

Non-trivial solutions($\vec{C_n} \neq 0$) to Eq. 2.12 require that no inverse matrix exists for $\widetilde{H} - E_n\widetilde{S}$ and this is satisfied by a vanishing determinant

$$det\Big[\widetilde{H} - E\widetilde{S}\Big] = 0 \tag{2.13}$$

which gives us the energies for a given wave vector $\mathbf{k}$. Let us now continue the discussion with the more generalized case of more than one basis atom and orbital, for which we only need to modify the basis set φ and the coefficients C in the wavefunction expansion

$$\varphi_{ji}(\mathbf{k}, \mathbf{r}) = \frac{1}{\sqrt{N}} \sum_{\mathbf{R}} e^{i\mathbf{k}.\mathbf{R}} \phi_j(\mathbf{r} - \mathbf{R} - \mathbf{t_i}), \quad |\psi\rangle = \sum_{ji} |\varphi_{ji}\rangle C_{ji} \tag{2.14}$$

Now, going back to Eq. 2.8 and Eq. 2.9 and substituting Eq. 2.3, for the Hamiltonian, we have

$$H_{nn'} = \frac{1}{N} \sum_{\mathbf{R}\mathbf{R}'} e^{-i\mathbf{k}.\mathbf{R}'} e^{i\mathbf{k}.\mathbf{R}} \langle \phi_{j'}(\mathbf{r} - \mathbf{R}' - \mathbf{t_{i'}}) | \hat{H} | \phi_j(\mathbf{r} - \mathbf{R} - \mathbf{t_i}) \rangle \tag{2.15}$$

where n, n' can be thought of as a combined index for both basis index and orbital index. If we define $\mathbf{R}'' \equiv \mathbf{R} - \mathbf{R}'$, and shift the arguments of $\phi(\mathbf{r})$ by $\mathbf{R}'$(which we can do since the Bloch phases resulting from translation cancel out), we have

$$\begin{aligned} H_{nn'} &= \frac{1}{N} \sum_{\mathbf{R}\mathbf{R}'} e^{i\mathbf{k}.(\mathbf{R}-\mathbf{R}')} \langle \phi_{j'}(\mathbf{r} - \mathbf{t_{i'}}) | \hat{H} | \phi_j(\mathbf{r} - (\mathbf{R} - \mathbf{R}') - \mathbf{t_i}) \rangle \\ &= \frac{1}{N} \sum_{\mathbf{R}\mathbf{R}''} e^{i\mathbf{k}.\mathbf{R}''} \langle \phi_{j'}(\mathbf{r} - \mathbf{t_{i'}}) | \hat{H} | \phi_j(\mathbf{r} - \mathbf{R}'' - \mathbf{t_i}) \rangle \\ &= \sum_{\mathbf{R}''} e^{i\mathbf{k}.\mathbf{R}''} \langle \phi_{j'}(\mathbf{r} - \mathbf{t_{i'}}) | \hat{H} | \phi_j(\mathbf{r} - \mathbf{R}'' - \mathbf{t_i}) \rangle \end{aligned} \tag{2.16}$$

where going from the first to the second line, the sum over $\mathbf{R}'$ has been switched to run over $\mathbf{R}''$ instead, and the independent sum evaluated over $\mathbf{R}$ then cancels out the $1/N$ factor. Following the same argument for $S_{nn'}$, we have

$$S_{nn'} = \sum_{\mathbf{R}''} e^{i\mathbf{k}.\mathbf{R}''} \langle \phi_{j'}(\mathbf{r} - \mathbf{t_{i'}}) | \phi_j(\mathbf{r} - \mathbf{R}'' - \mathbf{t_i}) \rangle \tag{2.17}$$

Fortunately for us, in the tight binding approximation, the integrals in these expressions need not be evaluated. Instead, they are fitted to either experimental data or values gathered from more rigorous approaches. Starting with the integral in the expression for $S_{nn'}$, we have

$$\langle \phi_{j'}(\mathbf{r} - \mathbf{t_{i'}}) | \phi_j(\mathbf{r} - \mathbf{R}'' - \mathbf{t_i}) \rangle = \delta(\mathbf{R}'')\delta_{jj'}\delta_{ii'} + \mathcal{S}_{jj',ii'}\delta((\mathbf{R}'' + \mathbf{t_i} - \mathbf{t_{i'}}) - \mathbf{d}_{nn}) \tag{2.18}$$

where $\mathcal{S}_{jj',ii'}$ are the overlap parameters and $\mathbf{d}_{nn}$ is the vector extending to the nearest neighbor. More often than not, these overlaps are considered negligible so the overlap parameters are taken to be zero, resulting in the identity matrix.

Similarly, for $H_{nn'}(\mathbf{k})$ we have

$$\begin{aligned} \langle \phi_{j'}(\mathbf{r} - \mathbf{t_{i'}}) | \hat{H} | \phi_j(\mathbf{r} - \mathbf{R}'' - \mathbf{t_i}) \rangle = \epsilon_{j,i}\delta(\mathbf{R}'')\delta_{jj'}\delta_{ii'} \\ + \mathcal{V}_{jj',ii'}\delta((\mathbf{R}'' + \mathbf{t_i} - \mathbf{t_{i'}}) - \mathbf{d}_{nn}) \end{aligned} \tag{2.19}$$

where $\epsilon_{j,i}$ can be thought of as the on-site energy of orbital j on basis atom i, and $\mathcal{V}_{jj',ii'}$ are called the transfer or hopping parameters and these parameters essentially define the strength of the bond between the j orbital on atom i and j' orbital on atom i'. Assuming that there are a total of N atoms in the unit cell, and J orbitals on each atomic site, our transfer and overlap matrices will have dimensions $(N * J) \times (N * J)$. With these simplifications, building these matrices is almost a trivial task and one can calculate the band structure by solving Eq. 2.13 for a set of $\mathbf{k}$-points.

Thee next-nearest neighbor interactions can also be included with minimal effort with a suitable hopping parameter[31], which, in the case of graphene, results in interactions between same type atoms, contributing to the diagonal elements of the Hamiltonian. However, including the next-nearest neighbors do not significantly improve the accuracy of the method[32].

In order to illustrate the steps outlined above, and to reference later for comparison, let us have a look at an example; the 2D square lattice.

2.1.1 Example: Square Lattice with Single Atom Basis

Let us consider the case where only a single interacting s orbital is taken into account for a single basis atom in a square lattice with lattice spacings given by a. We will also restrict our discussion to nearest neighbor interactions. The crystal wavefunction is simply given as

$$\begin{aligned}\psi(\mathbf{k},\mathbf{r}) &= \sum_{ji} C_{ji}(\mathbf{k})\phi_{ji}(\mathbf{k},\mathbf{r}) \\ &= C_{1s}(\mathbf{k})\psi_{1s}(\mathbf{k})\end{aligned} \tag{2.20}$$

which is just one term since there is a single s orbital on a single basis atom. The Hamiltonian of the system is then just a 1×1 matrix

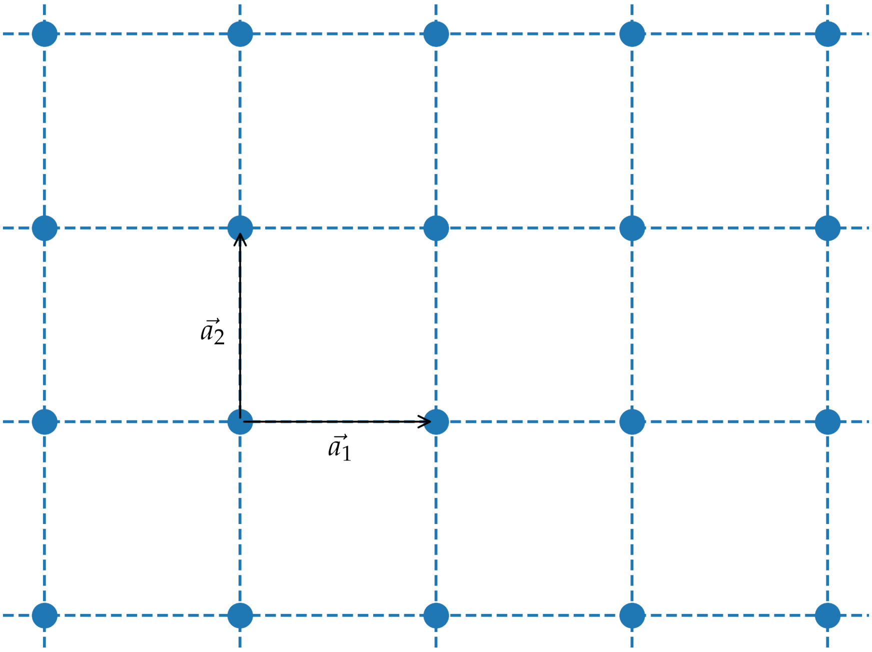

Figure 2.1: Square lattice with a single atom basis, where a_1 and a_2 are the primitive lattice vectors.

$$\begin{aligned}H &= \sum_{\mathbf{R}} e^{i\mathbf{k}.\mathbf{R}}\Big[\epsilon_{1s}\delta(\mathbf{R}) + \mathcal{V}_{ss}\delta(\mathbf{R}-\mathbf{d}_{nn})\Big] \\ &= \epsilon_{1s} + \mathcal{V}_{ss}\big[e^{ik_xa} + e^{-ik_xa} + e^{ik_ya} + e^{-ik_ya}\big] \\ &= \epsilon_{1s} + 2\mathcal{V}_{ss}\big[cos(k_xa) + cos(k_ya)\big]\end{aligned} \tag{2.21}$$

A plot these energies on a reciprocal space grid can be seen in Fig. 2.2

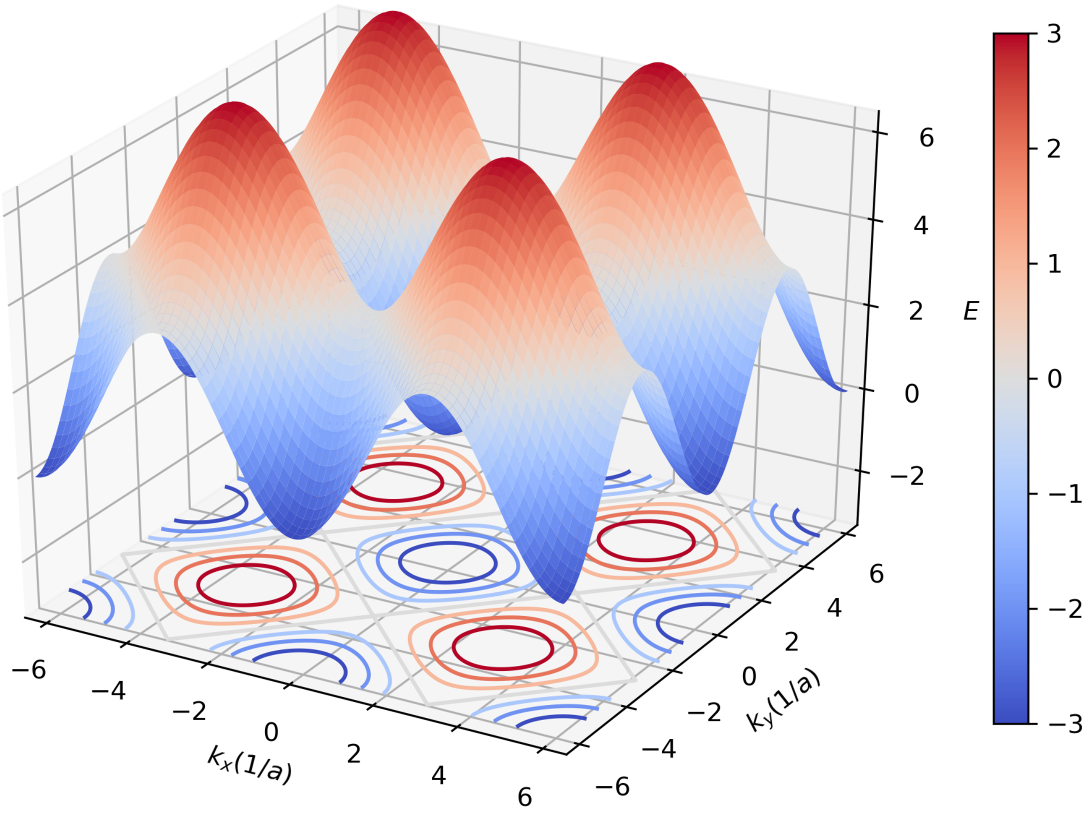

Figure 2.2: Square lattice energies plotted on a k_x/k_y grid with $k_x, k_y \in [-2\pi/a, 2\pi/a]$, with ϵ_{1s} taken to be zero.

2.1.2 Example: Primitive cell of graphene with only p_z orbitals

The most important electronic properties of graphene are known to be determined by the interaction of p_z orbitals. In this example, we only consider single p_z orbitals contributed by two inequivalent atoms in the smallest possible unit cell of graphene. Therefore, we have two terms in the sum expressing the crystal wavefunction 2.5

$$\begin{aligned}\psi_{\mathbf{k}}(\mathbf{r}) &= \sum_{mi} C_{\mathbf{k}mi}\phi_{\mathbf{k}mi}(\mathbf{r}) \\ &= C_{\mathbf{k}p_z,A}\psi_{\mathbf{k}p_z,A} + C_{\mathbf{k}p_z,B}\psi_{\mathbf{k}p_z,B}\end{aligned} \tag{2.22}$$

where the subscripts A and B denote the basis index. Dropping the p_z subscripts for simplicity, the transfer and the overlap matrices in Eq. 2.12 form 2×2 matrices of the form

$$\widetilde{H} = \begin{pmatrix} \langle\psi_A|H|\psi_A\rangle & \langle\psi_A|H|\psi_B\rangle \\ \langle\psi_B|H|\psi_A\rangle & \langle\psi_B|H|\psi_B\rangle \end{pmatrix} \quad \widetilde{S} = \begin{pmatrix} \langle\psi_A|\psi_A\rangle & \langle\psi_A|\psi_B\rangle \\ \langle\psi_B|\psi_A\rangle & \langle\psi_B|\psi_B\rangle \end{pmatrix} \tag{2.23}$$

Let us now evaluate one of the terms, the upper off-diagonal one, according to Eq. 2.19

$$\begin{aligned}\langle\psi_A|H|\psi_B\rangle &= \mathcal{V}_\pi[1 + e^{i\mathbf{k}.(-\frac{\mathbf{a}}{\mathbf{2}}\hat{\mathbf{i}}+\frac{\mathbf{a}\sqrt{\mathbf{3}}}{\mathbf{2}}\hat{\mathbf{j}})} + e^{i\mathbf{k}.(-\frac{\mathbf{a}}{\mathbf{2}}\hat{\mathbf{i}}-\frac{\mathbf{a}\sqrt{\mathbf{3}}}{\mathbf{2}}\hat{\mathbf{j}})}] \\ &= \mathcal{V}_\pi[1 + e^{-ik_xa/2}e^{ik_ya\sqrt{3}/2} + e^{-ik_xa/2}e^{-ik_ya\sqrt{3}/2}] \\ &= \mathcal{V}_\pi[1 + 2e^{-ik_xa/2}cos(k_ya\sqrt{3}/2)]\end{aligned} \tag{2.24}$$

Since $\widetilde{H}$ has to be a hermitian matrix, $\langle\psi_B|H|\psi_A\rangle$ is found trivially. Assuming only nearest neighbor interactions, atom type A has no A-type neighbors and the diagonal terms are simply on-site energies and just cause a shift in the band energies. Setting up the transfer and overlap matrices for points on a reciprocal space grid, we arrive at the well known band structure for graphene in Fig. 2.3. Dirac points - where the valence and conduction bands meet - can be seen at the vertices of the hexagonal Brillouin zone, **K** and **K**′ high symmetry points.

2.2 Tight Binding Method Under a Magnetic Field

The first study of charged particles under the effects of both a periodic potential and external magnetic field dates back to 1933 when R. Peierls hypothesized that one

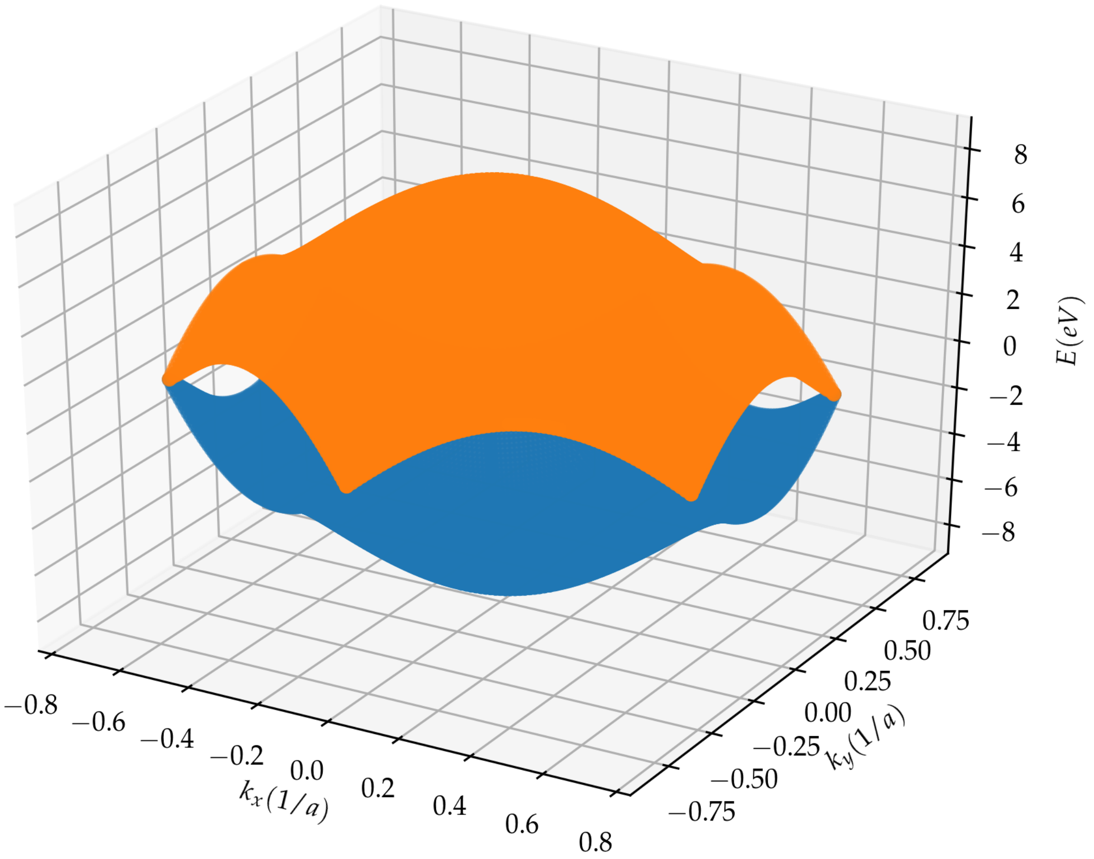

Figure 2.3: Graphene band structure on a k_x/k_y grid formed on the 1^{st} Brillouin zone.

could first solve the problem for $B = 0$ and then substitute the mechanical momentum operator into the dispersion relation[33]. Peierls substitution states that, under a magnetic field given by a vector potential $\mathbf{A}(\mathbf{r})$, one can transform the hopping parameters as

$$\mathcal{V}_{mm'} \rightarrow \mathcal{V}_{mm'}\, e^{i\frac{e}{\hbar}\int_{m}^{m'} \mathbf{A}(\mathbf{r}).\mathbf{dl}} \tag{2.25}$$

where the line integral is to be taken on the straight line connecting two atoms. This phase factor is a manifestation of the Aharonov-Bohm phases a charged particle experiences while moving under a magnetic field[34]. This substitution is valid as long as the vector potential $\mathbf{A}$ varies slowly on the scale of the lattice. A derivation and justification is given in Appendix A.

Working through the square lattice example in Section 2.1.1 by transforming the hopping parameters may seem like a straightforward way to solve the problem under a magnetic field but one has to be careful. The spatial dependence of the vector potential $\mathbf{A}(\mathbf{r})$ breaks the invariance of the Hamiltonian under translation by the lattice vectors since they also translate the argument of the vector potential. Because of this, we can no longer work with the same lattice vectors, and hence the unit cell. Let us now work through the square lattice example in order to find a way around this issue.

2.2.1 Example: Square Lattice Under Uniform $\vec{B}$

In order to introduce a magnetic field, we have to define a corresponding vector potential. However, there are infinitely many choices since the vector potential is only defined up to a gradient term. This gives us the freedom to hand pick a vector potential in order to make our calculations easier as long as the curl gives correct magnetic field. In the following discussion, we will be using the Landau gauge $\mathbf{A} = (0, Bx, 0)$ so that $\mathbf{B} = \nabla \times \mathbf{A} = B\hat{k}$. For convenience, let us switch to a shorthand notation for these extra terms and define

$$\theta_{m,n}^{m',n'} \equiv -\frac{e}{\hbar}\int_{m,n}^{m',n'} \mathbf{A}.\mathbf{dl} \tag{2.26}$$

With the given Landau gauge, the line integral $\int \mathbf{A}.\mathbf{dl}$ is evaluated to $\int Bxdy$. Let us now express the Hamiltonian from the zero-field example with the transformed hopping parameters, assuming that our atom has site indices (m, n)

$$H = \mathcal{V}_{ss}\left[e^{ik_xa}e^{i\theta_{m,n}^{m+1,n}} + e^{-ik_xa}e^{i\theta_{m,n}^{m-1,n}} + e^{ik_ya}e^{i\theta_{m,n}^{m,n+1}} + e^{-ik_ya}e^{i\theta_{m,n}^{m,n-1}}\right] \tag{2.27}$$

Since $dy = 0$ along the x direction, $\theta_{m,n}^{m\pm1,n} = 0$, and since $x = ma$ for the given lattice site, $\theta_{m,n}^{m,n\pm1} = \pm\frac{e}{\hbar}Bma^2$. Identifying Ba^2 as the magnetic flux Φ passing through the unit cell and h/e as the flux quantum Φ_0, we have

$$H = \mathcal{V}_{ss}\left[e^{ik_xa} + e^{-ik_xa} + e^{ik_ya}e^{i2\pi\frac{\Phi}{\Phi_0}m} + e^{-ik_ya}e^{-i2\pi\frac{\Phi}{\Phi_0}m}\right] \tag{2.28}$$

So, the Hamiltonian depends on the site index m and the translational invariance along the x axis is broken. In order to restore this invariance, we can look at the case where the ratio of magnetic flux and flux quanta is a rational number $\Phi/\Phi_0 = p/q$. When this happens, the Hamiltonian becomes invariant under translations by an integral multiple of q cells along x-axis, allowing us to define what we will call the magnetic unit cell in Fig. 2.4. Instead of the regular lattice vectors $\mathbf{a_1} = a\hat{i}$ and $\mathbf{a_2} = a\hat{j}$ for

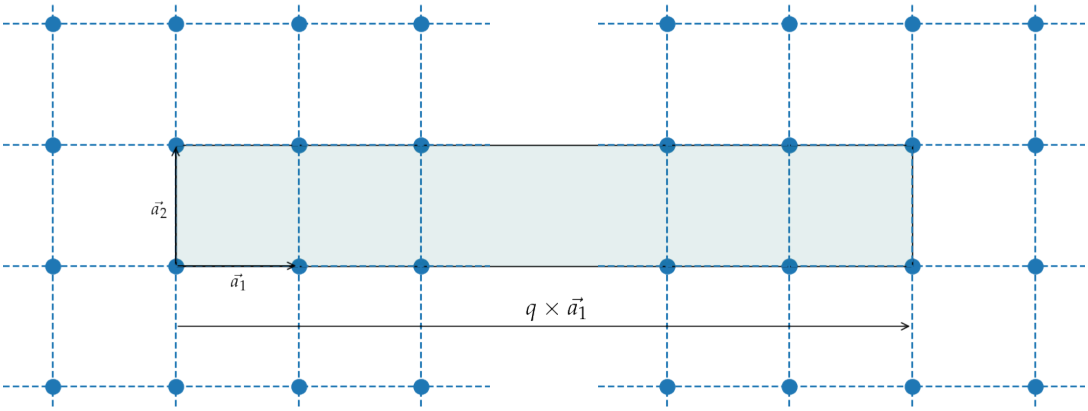

Figure 2.4: Magnetic unit cell for square lattice with single atom basis. The primitive cell is enlarged in $\mathbf{a_1}$ direction and this direction is decided by the Landau gauge used in the problem.

the unit cell in the zero-field case, the magnetic unit cell has lattice vectors $\mathbf{a_1} = qa\hat{i}$ and $\mathbf{a_2} = a\hat{j}$ and translational invariance is restored for a Hamiltonian expressed for this enlarged unit cell. As a result, we have a $q \times q$ Hamiltonian for our magnetic unit cell which can be constructed following the procedure given in Section 2.1.

Now, for a given flux ratio p/q, only the q value determines the periodicity of the magnetic unit cell assuming p and q are mutually prime numbers. When we plot the band energies while varying p, we arrive at the famous Hofstadter butterfly[35], a complex fractal structure as seen in Fig. 2.5. This structure is generated at the $\Gamma = (0, 0, 0)$ k-point. This fractal spectrum is a result of two competing effects, lattice periodicity and magnetic unit cell periodicity enforced by the presence of the magnetic field.

An alternative approach to the derivation of the Hamiltonian under a magnetic field is given in Appendix B. One might ask what happens when p/q is an irrational number. In that case, the magnetic unit cell is of infinite size and the spectrum is a zero-measure Cantor set. This case is studied thoroughly in Hofstadter's work[35].

When we shift our discussion from uniform fields to our main focus, localized fields, we have to define a suitable vector field and this quickly becomes a cumbersome task. To that end, we will use a gauge that works for even the most arbitrary fields.

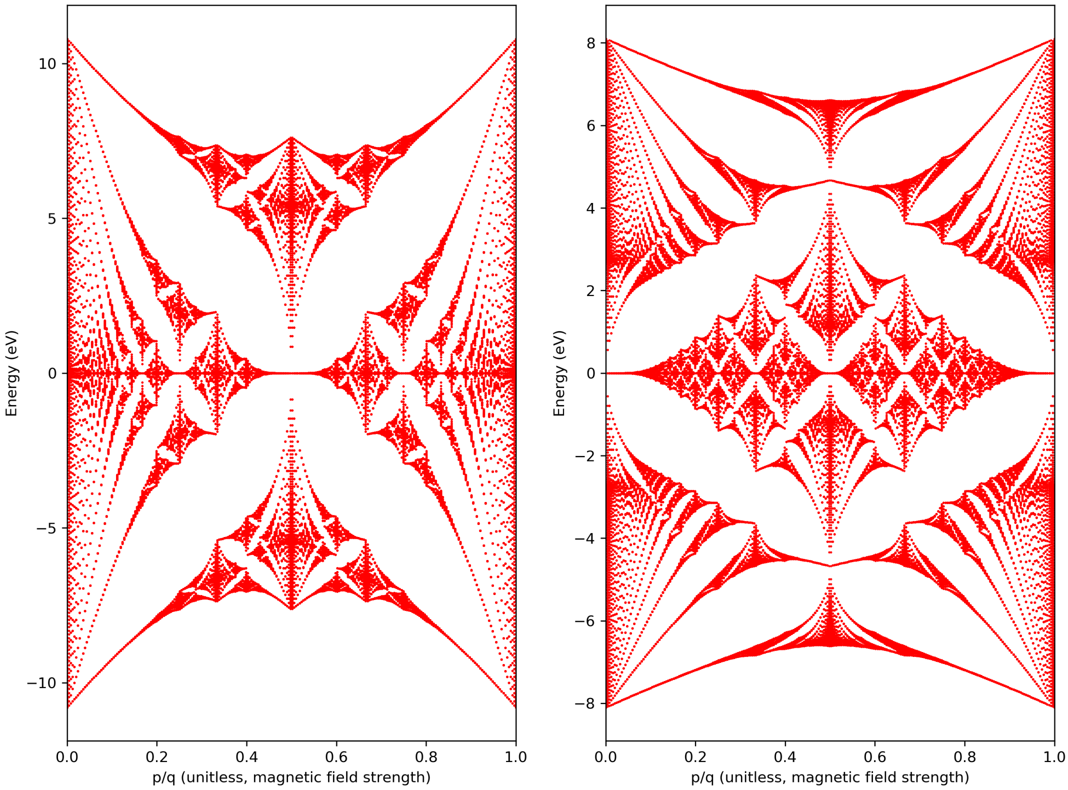

Figure 2.5: Hofstadter's butterfly for square(left) and hexagonal(right) lattices with $q = 151$.

2.2.2 The Optimal Gauge

Our reasoning in choosing the Landau gauge over other choices such as the symmetric gauge was that the Landau gauge simplifies the calculations. However, is it not always clear what gauge one should choose for more complex magnetic field distributions. In fact, for an arbitrary magnetic field, finding a vector potential can be a very challenging task. Gauge freedom comes to our aid at this point and provides us with a very convenient solution.

In order to understand this freedom, we can note that the only requirement on $\mathbf{A}$ is the closed loop integral being equal to the magnetic flux passing through a surface whose boundary is given by the closed loop. This can be expressed as

$$\oint_{\partial S} \mathbf{A}.\mathbf{dl} = \int_S \mathbf{B}.\mathbf{dS} \tag{2.29}$$

This simple requirement lets us choose very efficient gauges. In fact, instead of

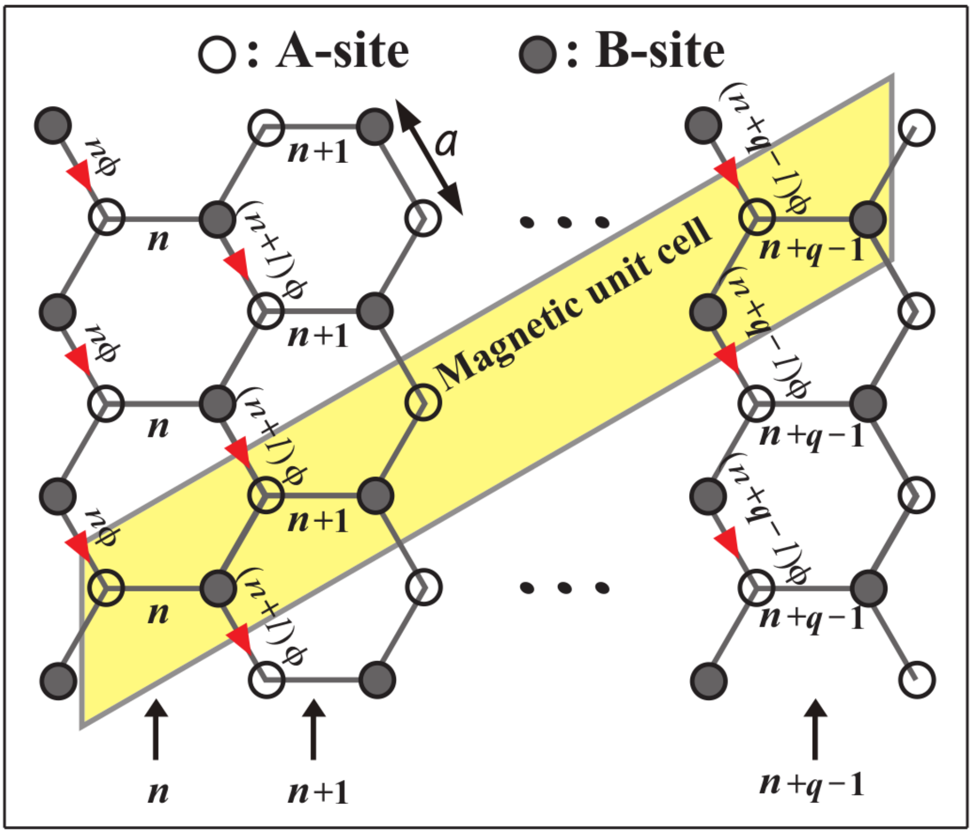

Figure 2.6: Optimal gauge for graphene: only the line integrals over the paths with red arrows are set to be non-zero. Values for the non-zero line integrals are given by the destination hexagon's x-index n. Reprinted from [1]

choosing a gauge, we can choose values for the line integrals themselves, as long as the total line integral over any closed loop gives the correct magnetic flux. This choice of gauge is called the optimal gauge[36] because the size of the magnetic unit cell is minimal with this type of gauge.

The simplification brought by this gauge can be appreciated by revisiting the graphene under uniform field example in Fig. 2.6. In the case of graphene, this gauge essentially cuts down the minimum possible size of the magnetic unit cell by a factor of 2. While uniform fields can easily be treated in this manner, this gauge works especially well if one wants to incorporate inhomogeneous fields into the tight binding method.

2.2.3 Inhomogeneous Fields

Using the efficient yet simple gauge called the optimal gauge explained in Section 2.2.2, the treatment for inhomogeneous fields follows in a very straightforward manner. For example, given a magnetic field completely localized on a cell in a square lattice(Fig. 2.7(a)), it suffices to set all the line integrals $\int \mathbf{A}.\mathbf{dl}$ above the cell to the value of the flux Φ passing through this cell and all others to zero. We can express this as

$$\theta_{m,n}^{m',n'} = \begin{cases} \Phi_1 & m' = m+1 \; and \; n' > n_1 \\ 0 & \text{otherwise} \end{cases} \tag{2.30}$$

The case of more than one such "flux tube" can be treated independently. For two separate flux tubes located on the same vertical slice as seen in Fig. 2.7(b), we can sum up the contributions separately so that

$$\theta_{m,n}^{m',n'} = \begin{cases} \Phi_1 + \Phi_2 & m' = m+1 \; and \; n' > n_2 \\ \Phi_1 & m' = m+1 \; and \; n_2 > n' > n_1 \\ 0 & \text{otherwise} \end{cases} \tag{2.31}$$

Since the flux distribution from an arbitrary magnetic field can be thought of as the sum of individual flux tubes, one only needs to calculate the flux values on each cell, and modify the hopping parameters accordingly. Using this tool, arbitrary fields can be studied, including sinusoidal, Gaussian centered on a given lattice site and so on. In this work, we will be studying two such cases, with details given in the next chapter.

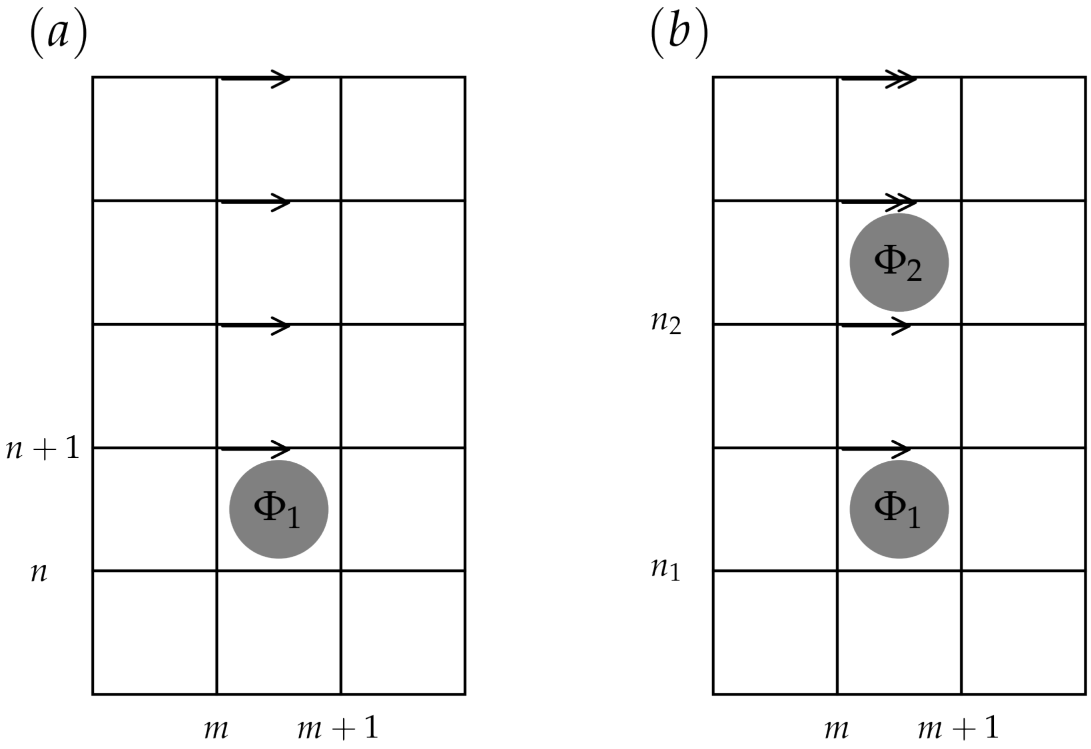

Figure 2.7: (a) A localized magnetic field creates a flux Φ_1 on a single cell. All the line integrals on the hopping paths above this cell are set to Φ_1. (b) Separate magnetic fields can be treated independently. If they are located on the same vertical slice, the line integrals are set to $\Phi_1 + \Phi_2$ above the upper cell, Φ_1 between, and 0 otherwise.

CHAPTER 3

CALCULATION DETAILS

We are currently developing a Python tight-binding module with which all the calculations have been performed. Source codes will be provided to interested readers upon request.

3.1 The Systems Investigated

The systems used in this study are all zero-dimensional graphene nanostructures; hexagonal flakes, Y-shaped junctions and two graphene nanoribbons forming a cross which can be seen in Fig. 3.2. Since mostly the π bands are responsible for the electronic properties of graphene, only the interactions between p_z orbitals have been taken into account with a corresponding hopping parameter of $V_{pp\pi} = -2.7eV$[31]. Bonds at the edges are assumed to be passivated by hydrogen atoms and do not contribute to the electronic states.

Even though the implementation of the optimal gauge(Section 2.2.2) is trivial for nearest-neighbor hopping, defining correct hopping values for the next-nearest neighbors proved to be a challenge. For this reason, as a first approximation, only the nearest neighbor hopping is used. Overlap is assumed to be negligible between neighboring orbitals so that the overlap matrix is taken to be the identity matrix. One can modify these parameters for more accurate results at the cost of computation time. For a set of tight-binding parameters that reproduces density functional theory(DFT) results, reader can refer to [31].

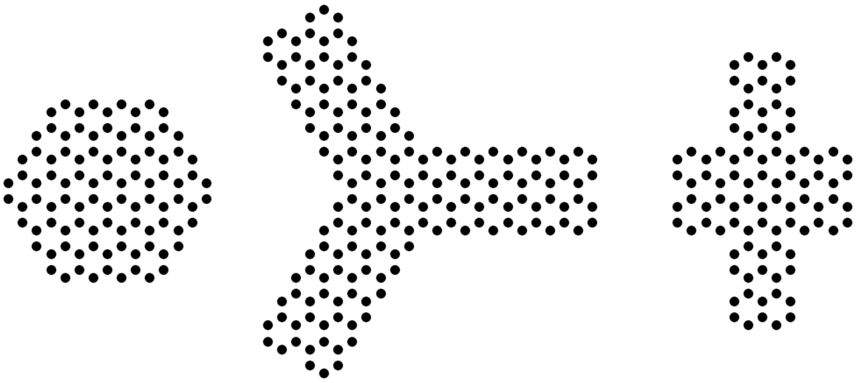

Figure 3.1: Three main graphene nanostructures used in this study. Only one edge variants are shown here.

3.1.1 Neighbor Table

The regular approach of defining a cutoff radius and defining all the atoms within this radius centered on a given atom turned out to be the bottleneck in the first versions of our code. In order to deal with this, one can recognize that the hexagonal lattice is topologically equivalent to brick lattice and can then form the neighbors using the indices on the brick lattice. For example, a given atom at lattice point with indices (m, n) always has neighbors at sites $(m, n-1)$ and $(m, n+1)$ and a third neighbor at either $(m+1, n)$ or $(m-1, n)$ and the sign just depends on the initial indexing of atoms. This cuts down cost of the neighbor table generating process considerably. This process can easily be generalized to include the next nearest neighbors. Nevertheless, we have added a module for calculating the neighbor list for future generalization efforts.

3.2 Density of States

Since we have finite systems, energy levels are discrete so the density of states will be composed of a series of delta functions located at each of the eigenvalues of the Hamiltonian. In order to simulate broadening effects such as electron-electron interactions, we will use a distribution function - Gaussian in this case - to calculate the

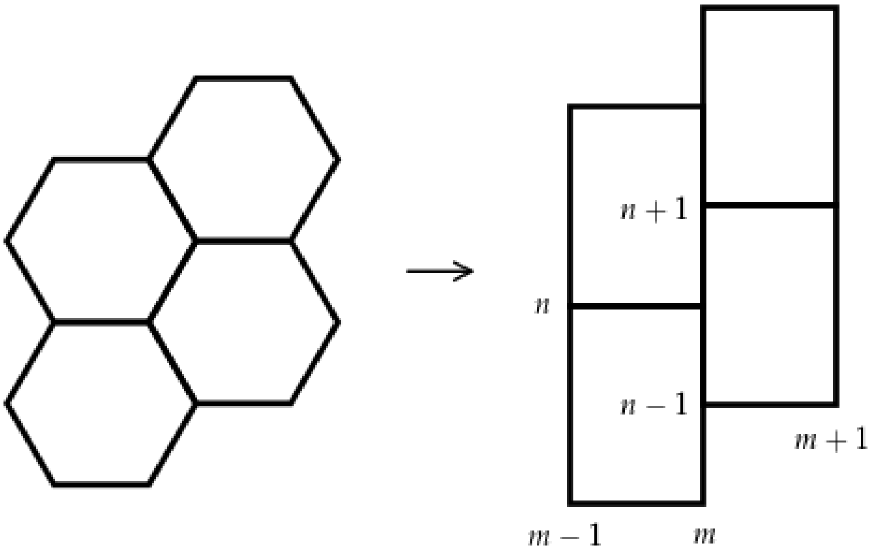

Figure 3.2: Mapping lattice points from hexagonal to an equivalent brick lattice.

density of states of our system.

$$\rho(E) = \sum_i D(E - \epsilon_i) \tag{3.1}$$

where ϵ_i are the eigenvalues of our Hamiltonian. Our energy values are in units of eV (not normalized to t) and unless stated otherwise, DOS plots will be generated with a set of 1000 energy values in the interval $[-8.1, 8.1]$ eV, which gives the full spectrum. For the Gaussian, σ is chosen to be $0.05eV$.

3.2.1 Projected(Local) Density of States

In order to investigate features in the DOS profiles in more detail, one can project the eigenstates onto specific atomic orbitals and calculate the individual contribution of orbitals to density of states in a given interval. The contribution of orbital ν to an energy value E is given by

$$\rho_\nu(E) = \sum_i {}_\nu\langle\psi_i|\big[S|\psi_i\rangle\big]_\nu D(E - \epsilon_i) \tag{3.2}$$

where ψ_i is the eigenvector of the i^{th} eigenvalue and the subscript ν implies projection onto orbital ν as $|\psi_i\rangle_\nu = \langle\psi_\nu|\psi_i\rangle|\psi_\nu\rangle$.

The reader should also keep in mind that in the following chapter, PDOS plots given are plotted using a colormap where the values increase as the color goes from light blue to red.

3.2.2 Magnetic Field

Results will be presented for three cases; (i) zero $\mathbf{B}$ (ii) $\mathbf{B} = B_0 g(x, y, \sigma)\hat{k}$ where $g(x, y, \sigma)$ is a Gaussian, and (iii) uniform $\mathbf{B}$. For case (ii), as a first approximation, we calculated the value of the Gaussian at the center of each hexagon and calculated the magnetic flux using that value. One can in fact work with any type of field distribution using the framework in Section 2.2.2.

CHAPTER 4

RESULTS

This chapter is organized as follows. We first present size dependence of density of state(DOS) profiles of our structures in zero-field regime. Then we will present both total and projected(local) density of states(PDOS) under localized and uniform magnetic fields for various structures. While the structures are quite different in their geometries, we will see that the corresponding DOS and PDOS plots show very similar results that is only dependent on the edge type.

For this reason, only the results for the hexagonal flakes and Y-shaped junctions will be presented. Y-shaped junctions will be denoted with a (A) or (Z) depending on the edge type along the arms, which represents the majority of edge types the junction is composed of. Y-shaped junctions present a mix of edge types so in a sense it is a more practical system than flakes since fabricating graphene nanostructures composed of only one type of edge is very difficult if not downright impossible.

For calculation details, please refer to Chapter 3.

4.1 Size Dependence of DOS

We start reviewing our results by first looking at the DOS profile of graphene flakes at varying sizes3.1.

Armchair flakes present an energy gap for small sizes and the this gap approaches zero with increasing flake size, as the flakes approach semi-metallic region4.1. This is in contrast to the case for the armchair nanoribbons where the structure has a zero energy gap whenever $W = 3M - 1$ - where W is the width of the nanoribbon in

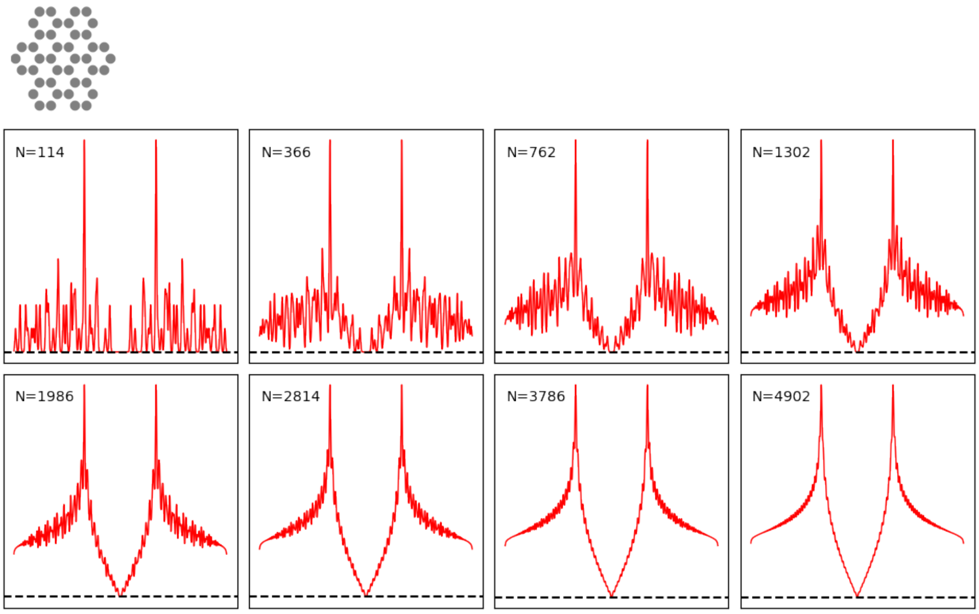

Figure 4.1: DOS of various sized armchair graphene flakes. Number in the top left is the number of atoms.

number of hexagons - and a non-zero gap otherwise[21]. For the armchair flakes, we found that the system starts out with a non-zero gap and the gap approaches zero as the size of the flake increases while the DOS profile converges to that of graphene.

Zigzag flakes on the other hand show a remarkable feature where a peak in the density of states emerges at the Fermi level $E = 0$[21] as seen in Fig. 4.2. This is due to the degenerate states arising at E=0. In fact, the number of such states is given by $N = |N_A - N_B|$ where N_A and N_B are the number of types of atoms A and B in the structure for a pure zigzag edged nanostructure[37].

Real nanoscale graphene networks have rather complicated structures composed of edges of both types. In order to see the combined effects of both edge types, we can use Y-shaped junctions where a mixture of both edge types are present. Looking at the DOS profile for Y-junction(A) in Fig.4.3, it can be seen that even small amounts of zigzag edges are enough to create new states around the Fermi level and since none were present in the armchair flake, these states are expected to be localized on the zigzag edges.

Y-junction(Z)(Fig. 4.4) shows a similar DOS profile to Y-junction(A)(Fig. 4.3). The

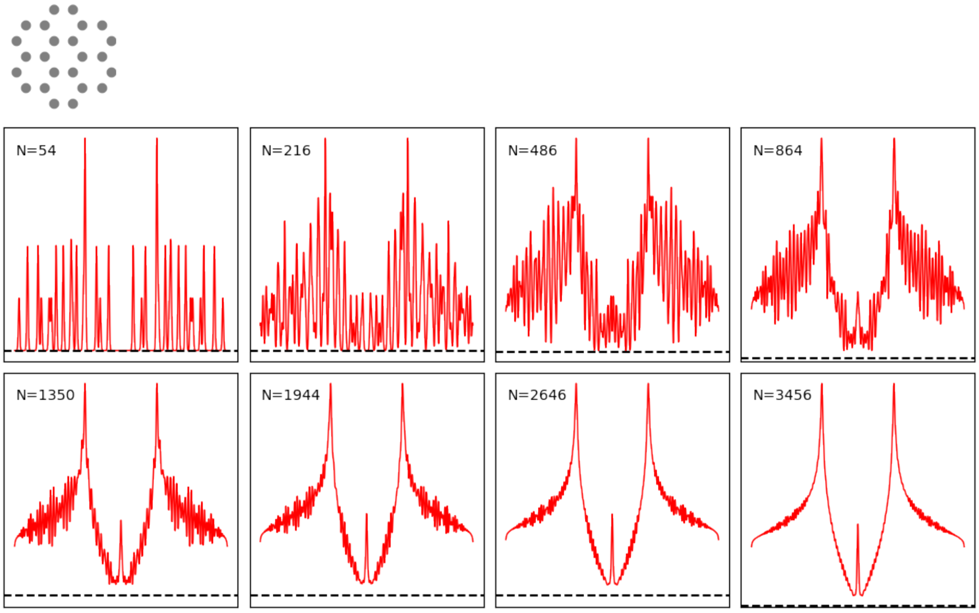

Figure 4.2: DOS of various sized zigzag graphene flakes. Number in the top left is the number of atoms.

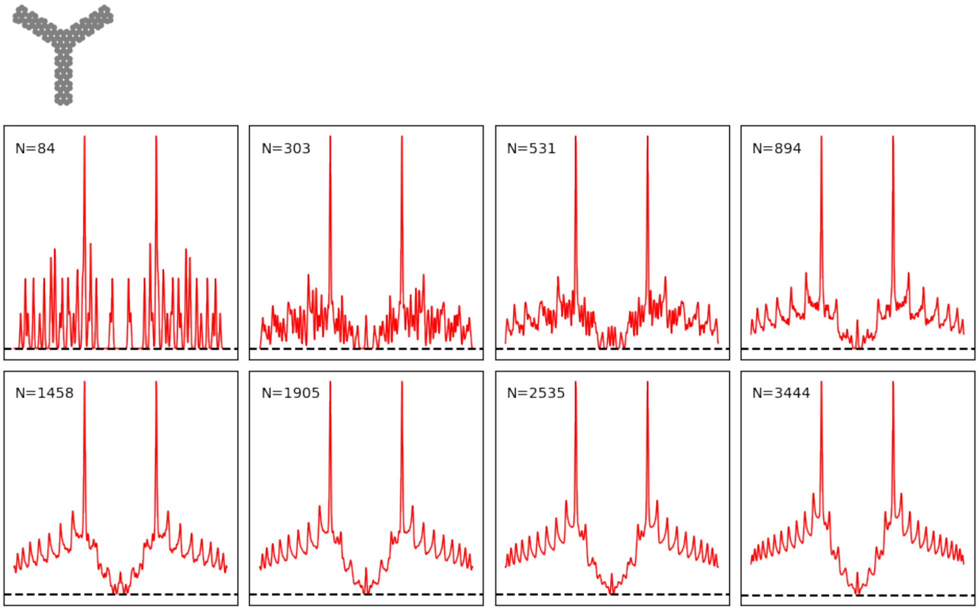

Figure 4.3: DOS of Y-shaped(A) junctions of varying sizes. Number in the top left is the number of atoms.

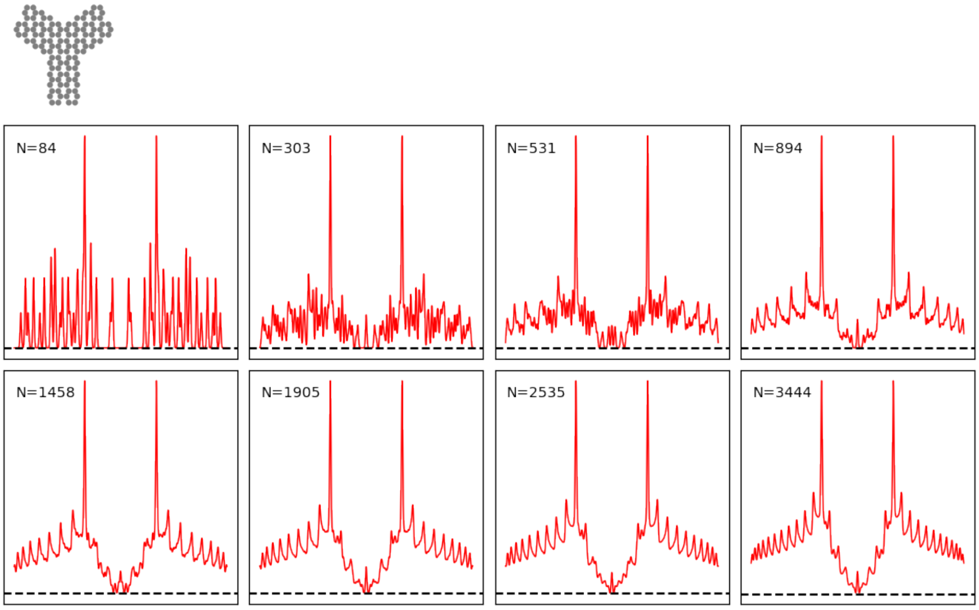

Figure 4.4: DOS of Y-shaped(Z) junctions of varying sizes. Number in the top left is the number of atoms.

more pronounced peak located at the Fermi level can be attributed to the higher number of zigzag edge atoms compared to Y-junction(A) case. Indeed, as the junction size increases, the DOS profile tends to that of a zigzag flake, as the zigzag/armchair edge ratio gets increasingly larger. Local density of states results in the following sections will show that the states around the Fermi level are localized on zigzag edges.

4.2 Hexagonal Flakes

Armchair flake, which is semi-metallic in the zero-field case, shows emergence of new states around the Fermi level when a magnetic field is applied, essentially turning the structure metallic as seen in Fig. 4.5. PDOS calculation shows new states around $E = 0$ that are localized on atoms where the magnetic field is applied, with the largest contributions coming from orbitals closer to the peak of the Gaussian.

As we have discussed earlier, zigzag flakes present new states around the Fermi level and PDOS calculation(Fig. 4.6) verifies that these states are located predominantly on edge sites. Under the localized magnetic field, the states around the Fermi level are enhanced while edge states remain untouched. The newly emerged states are

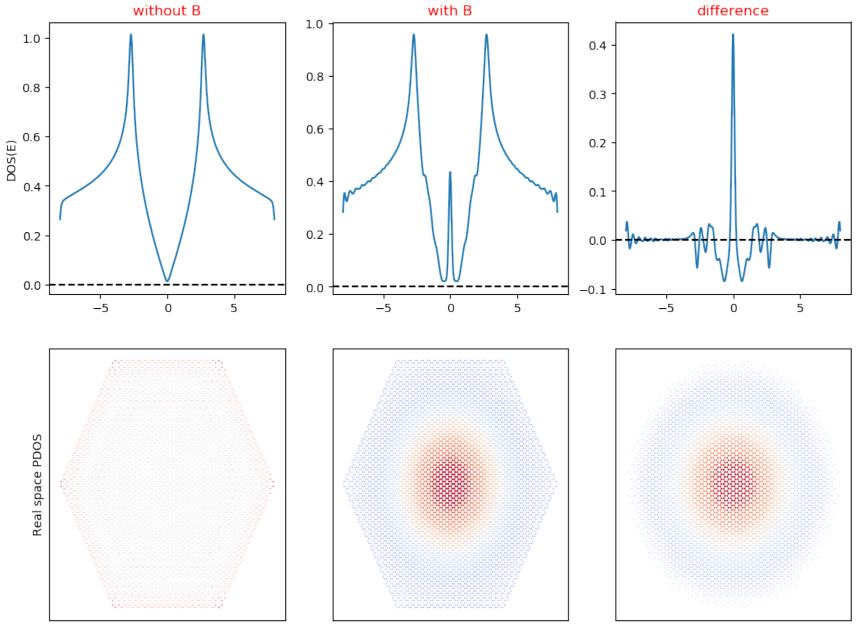

Figure 4.5: DOS(top) and PDOS(bottom) of armchair hexagonal flake with 5514 atoms. B-field Gaussian has a peak at (0,0) with magnitude 20T and σ is 20 angstroms.

localized near the Gaussian peak, similar to the armchair flake case.

Under a uniform field, the armchair flake presents a more distinct peak at the Fermi level compared to the localized field case(Fig. 4.5). Here, we see contribution to this peak from all atoms except those at the perimeter of the flake. Armchair edges can be specifically seen to not contribute to this peak under uniform magnetic field. There are apparent ripples in the density of states profile which can be attributed to Landau levels emerging due to the magnetic field. For a monolayer graphene, Landau level energies are given as $E_n = \sqrt{2e\hbar v_F^2 nB}$[38]. With $B = 20T$ and $v_F \approx 10^6 m/s$, Landau level spacing is roughly $0.50eV$.The periodicity of the ripples coincides with this value and the peaks we see are manifestation of Landau levels in Bloch bands.

Zigzag flake under a uniform field show almost the same DOS profile as the armchair flake, except for a slightly more pronounced peak at the Fermi level, due to the zero-field states localized at the edges as seen in Fig. 4.8. Both localized and uniform magnetic fields form new states at E=0 for both types of flakes and this enhancement is much more pronounced in the uniform field case.

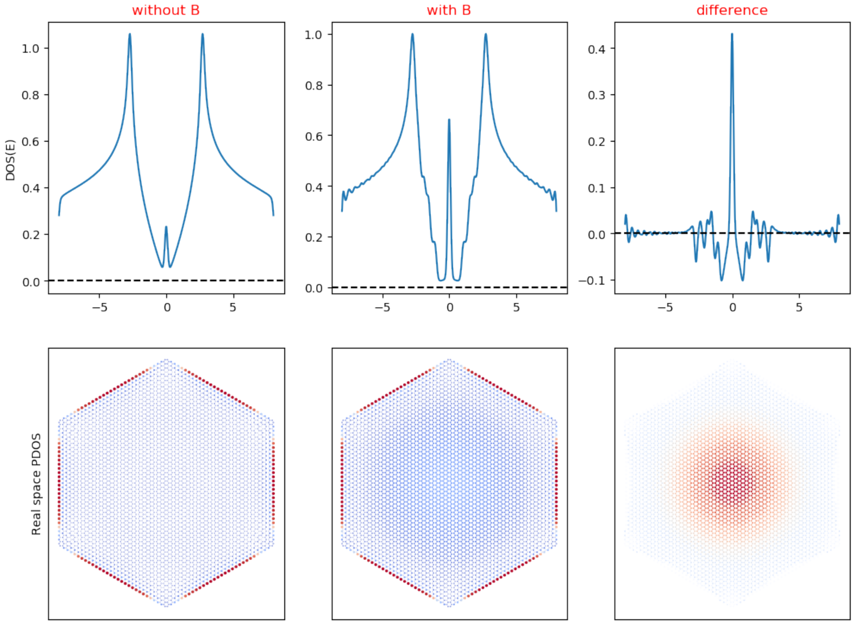

Figure 4.6: DOS(top) and PDOS(bottom) of zigzag hexagonal flake with 5400 atoms. B-field Gaussian has a peak at (0,0) with magnitude 20T and σ is 20 angstroms.

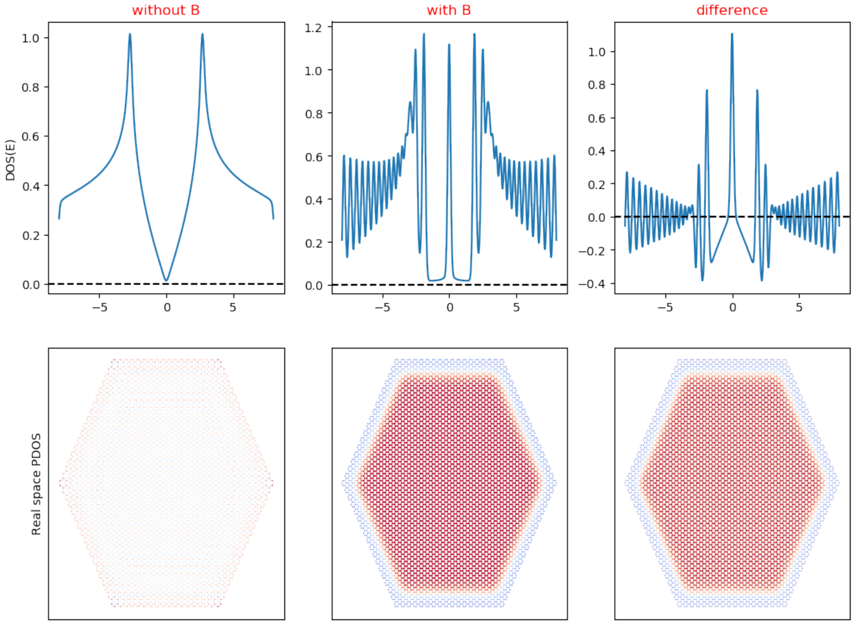

Figure 4.7: DOS(top) and PDOS(bottom) of armchair hexagonal flake with 5514 atoms. B-field is uniform with a magnitude of 20T.

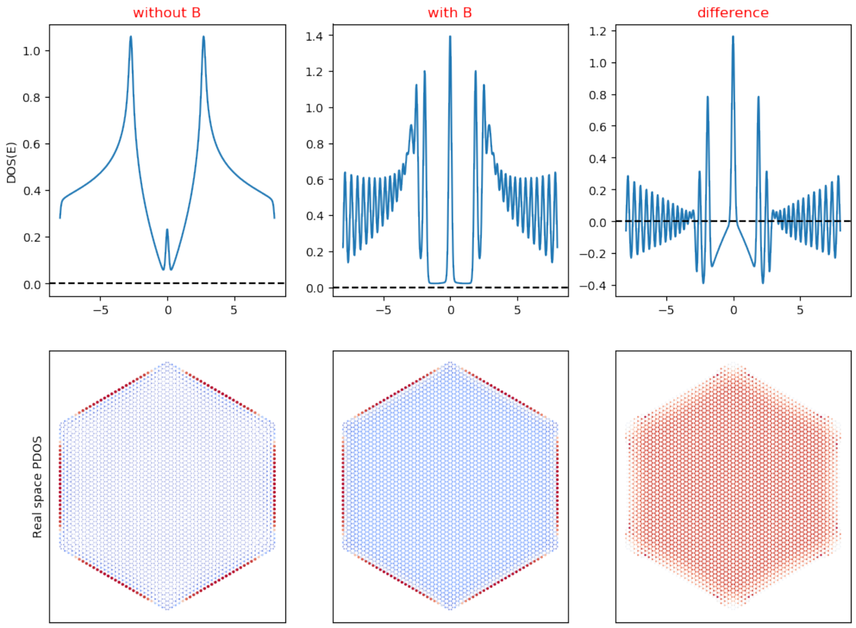

Figure 4.8: DOS(top) and PDOS(bottom) of zigzag hexagonal flake with 5400 atoms. B-field is uniform with a magnitude of 20T.

4.3 Y-shaped Junctions

As we have found earlier, Y-shaped(A) junction is metallic due to the presence of zigzag edges on the ends of the arms. The presence of a magnetic field enhances the states around the Fermi level just as it did for the hexagonal flakes. In fact, all the DOS/PDOS profiles(Figs. 4.94.104.114.12) show very similar behavior as the hexagonal flakes.

4.4 Cross-shaped Junctions

For sake of completeness, we present the DOS/PDOS results of cross-shaped junctions here. The seemingly asymmetric distribution of states for the Gaussian field case(Fig. 4.13) is just an artifact as a result of the aspect ratio of real space plots. The cross-shaped junction is actually much longer in x-direction and for a correct aspect ratio, the distribution of states is perfectly symmetric as we have seen for the other structures so far. Otherwise, since the profiles are very similar to those of flakes and Y-shaped junctions, the discussion will be skipped.

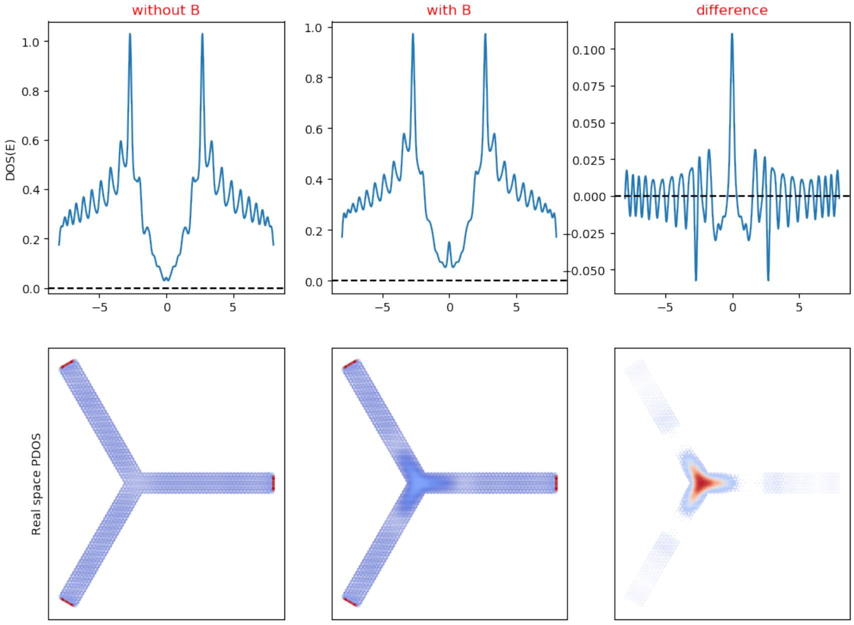

Figure 4.9: DOS(top) and PDOS(bottom) of Y-shaped(A) junction with 4929 atoms. B-field Gaussian has a peak at (0,0) with magnitude 20T and σ is 20 angstroms.

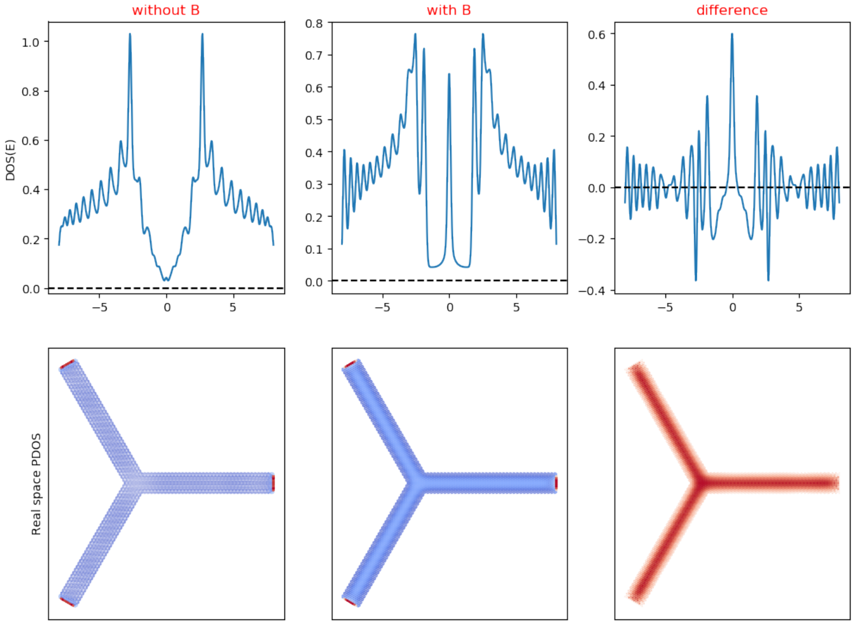

Figure 4.10: DOS(top) and PDOS(bottom) of Y-shaped(A) junction with 4929 atoms. B-field is uniform with a magnitude of 20T.

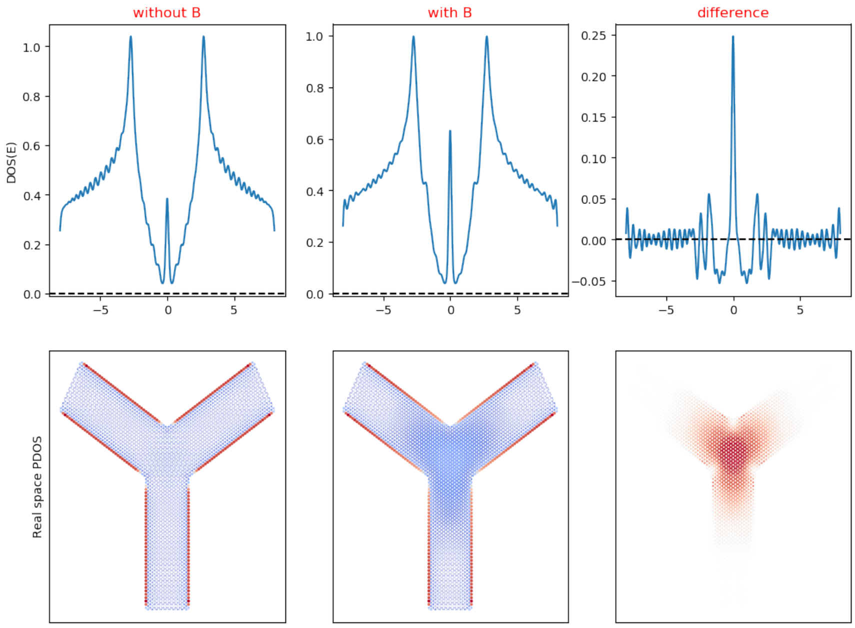

Figure 4.11: DOS(top) and PDOS(bottom) of Y-shaped(Z) junction with 5010 atoms. B-field Gaussian has a peak at (0,0) with magnitude 20T and σ is 20 angstroms.

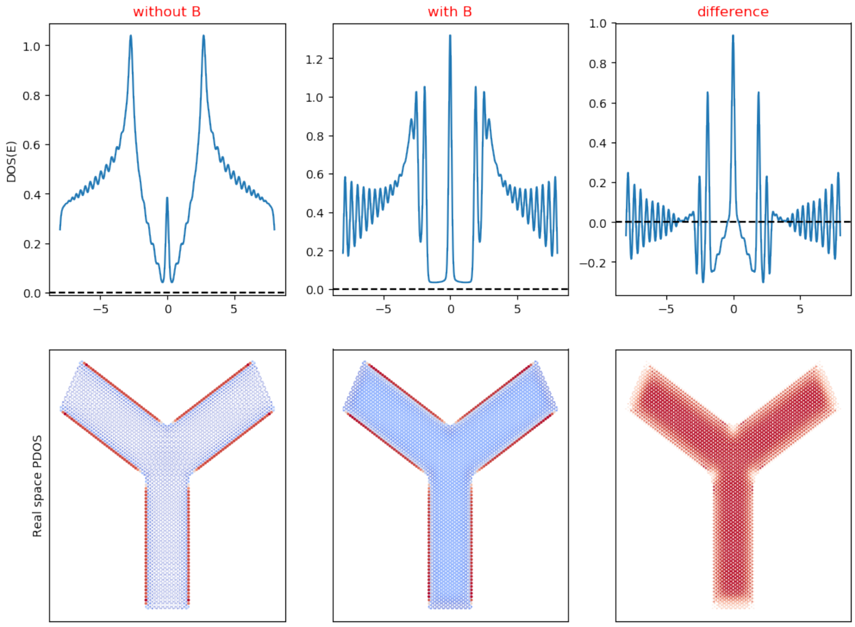

Figure 4.12: DOS(top) and PDOS(bottom) of Y-shaped(Z) junction with 5010 atoms. B-field is uniform with a magnitude of 20T.

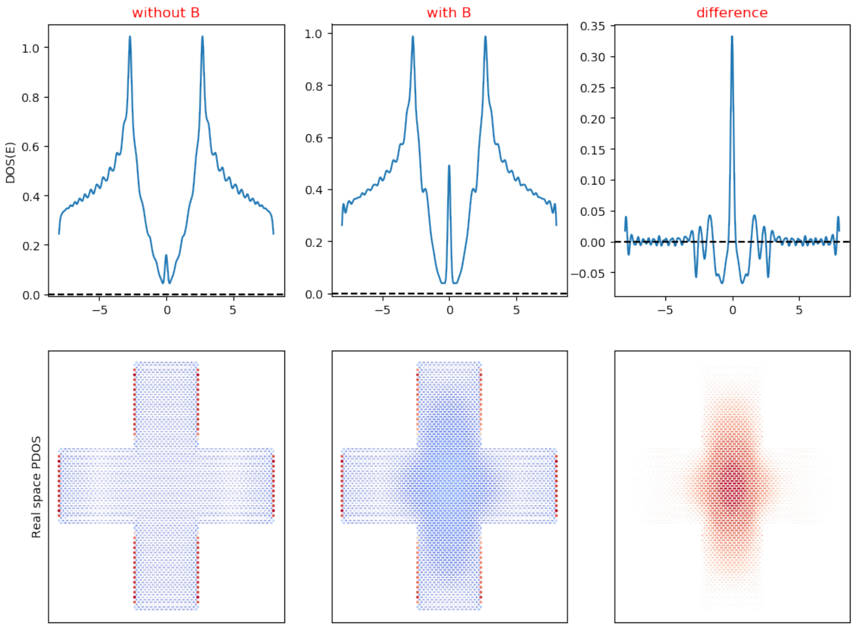

Figure 4.13: DOS(top) and PDOS(bottom) of cross-shaped junction with 5200 atoms. B-field Gaussian has a peak at (0,0) with magnitude 20T and σ is 20 angstroms.

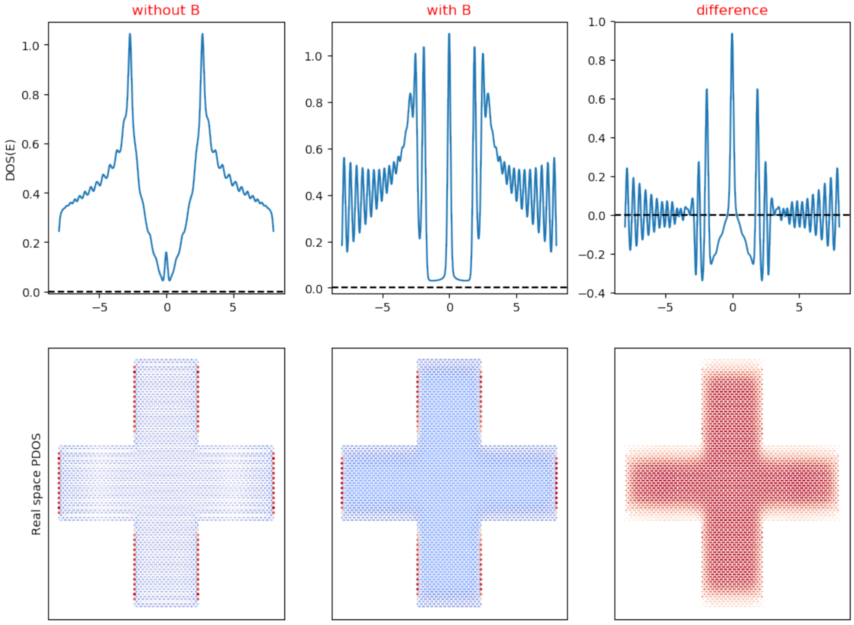

Figure 4.14: DOS(top) and PDOS(bottom) of Y-shaped(Z) junction with 5200 atoms. B-field is uniform with a magnitude of 20T.

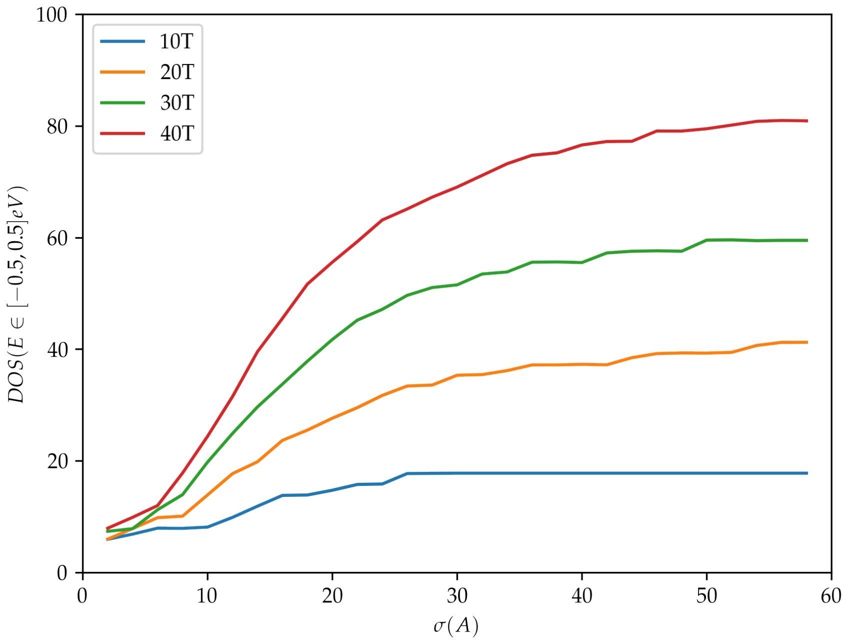

Figure 4.15: Number of states in interval [-0.5,0.5]eV as a function of σ for various magnetic field strengths on a an armchair hexagonal flake with 1014 atoms(hence orbitals). Here, the total DOS is normalized to the total number of orbitals in the lattice.

4.5 Magnetic Field Dependence of E=0 States

Since we are interested in the states near the Fermi level as they are responsible for important properties such as conductance at low temperatures, we can also look at how these states are affected under varying field distributions. Using an armchair hexagonal flake as our system of choice, we varied σ of the Gaussian for four different peak field magnitudes. Results show that as we have seen from DOS plots, as the magnetic field Gaussian tends to a uniform field with increasing σ, there are an increasing number of states emerging near the Fermi level. We see that there is a direct correlation between magnetic field strength and the number of emergent states with almost a linear relation in the uniform field limit as seen in armchair flake example in Fig. 4.15.

Zigzag flakes show the same profile except an positive offset in the number of Fermi level states(Fig. 4.16). This offset can be attributed to the inherent states present even

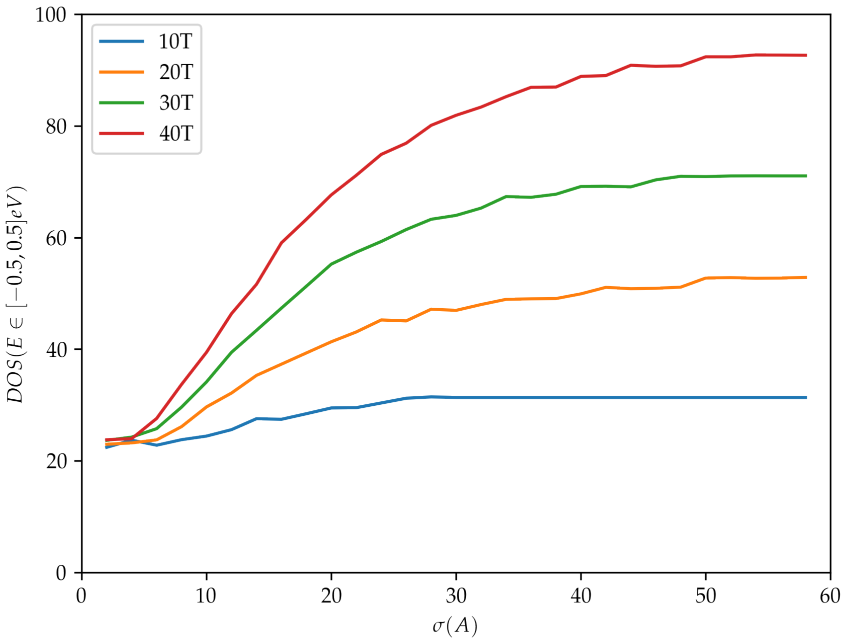

Figure 4.16: Number of states in interval [-0.5,0.5]eV as a function of σ for various magnetic field strengths on a an zigzag hexagonal flake with 1014 atoms(hence orbitals). Here, the total DOS is normalized to the total number of orbitals in the lattice.

in the zero-field case.

Y-shaped junctions show a similar profile, where the predominantly zigzag edged structure Y-junction(Z) starts off with a higher number of states near the Fermi level due to the edges(Fig. 4.18), apart from which the Gaussian width dependence is similar to that of Y-junction(A)(Fig. 4.17).

From these results, we see that while the magnetic field enhances the states near the Fermi level, and the type of edge plays no role looking solely on the effect of the magnetic field on these states.

4.6 Size Dependence of Fermi Level States

In this section, we look at the change in the states near the Fermi level as a function of structure size. For the armchair flakes, there is a linear relation between the applied

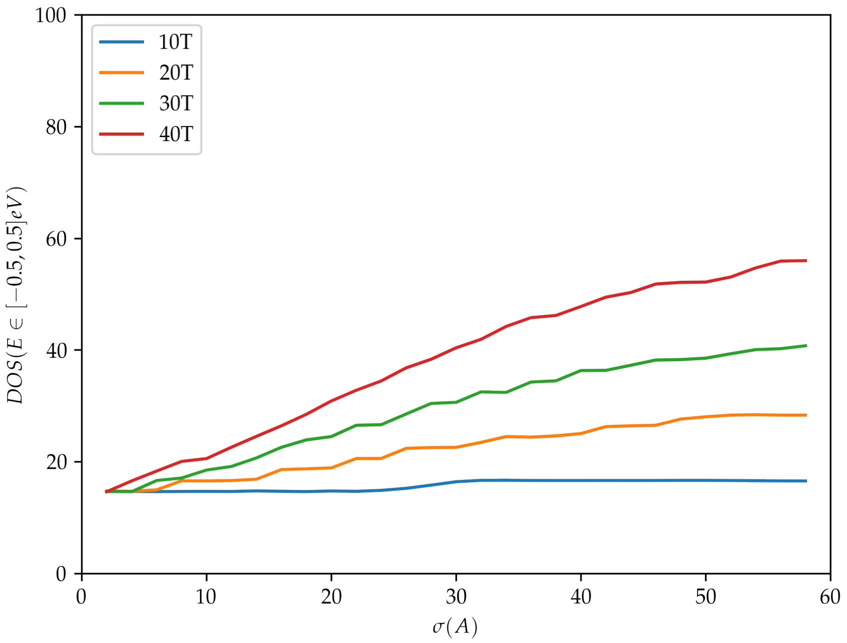

Figure 4.17: Number of states in interval [-0.5,0.5]eV as a function of σ for various magnetic field strengths on a Y-junction(A) with 927 atoms(hence orbitals). Here, the total DOS is normalized to the total number of orbitals in the lattice.

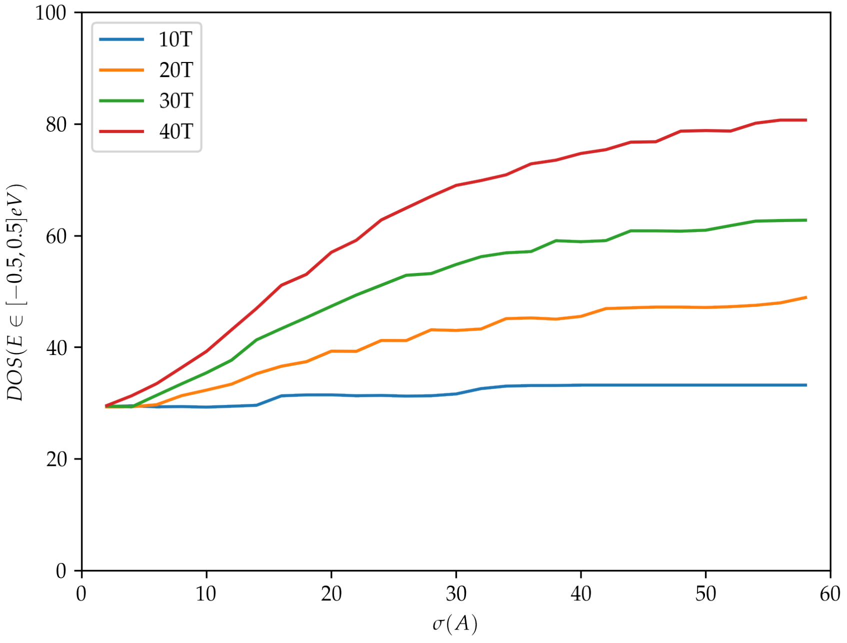

Figure 4.18: Number of states in interval [-0.5,0.5]eV as a function of σ for various magnetic field strengths on a Y-junction(Z) with 930 atoms(hence orbitals). Here, the total DOS is normalized to the total number of orbitals in the lattice.

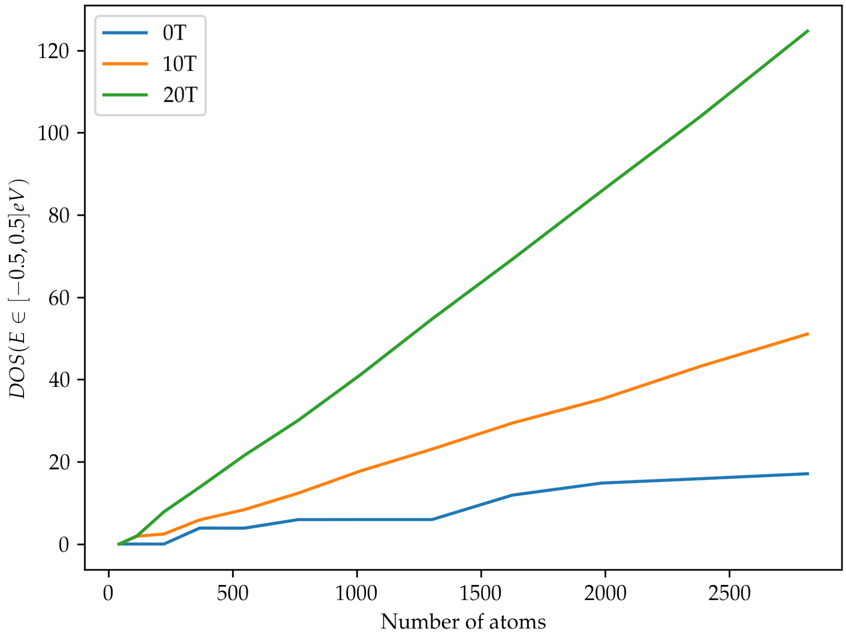

Figure 4.19: Number of states in interval [-0.5,0.5]eV as a function of number of atoms for various uniform magnetic field strengths on an armchair flake. Here, the total DOS is normalized to the total number of orbitals in the lattice.

magnetic field magnitude and the number of emergent states in the vicinity of the Fermi level as seen in Fig. 4.19. This is to be expected by looking at Fig. 4.15, where in the uniform field limit, the total number of emergent states converges to a constant value, which are uniformly distributed on all the atoms in the flake(Fig. 4.7). As the number of atoms increases, we expect that the number of such states to increase linearly as well. The zero-field case in Fig. 4.15 is a bit misleading since it shows localized states where there are no such states for the pure armchair flake. This is a result of summing the states in the interval [-0.5,0.5]eV which also counts the tails of the conduction and valence bands. Zigzag flake results in Fig. 4.20, show a similar trend. In fact, the difference in slopes of the lines with B=20T and B=0T for both the armchair and zigzag case gives the same value, verifying our assertion that the type of edge plays no role in the enhancement of states near the Fermi level.

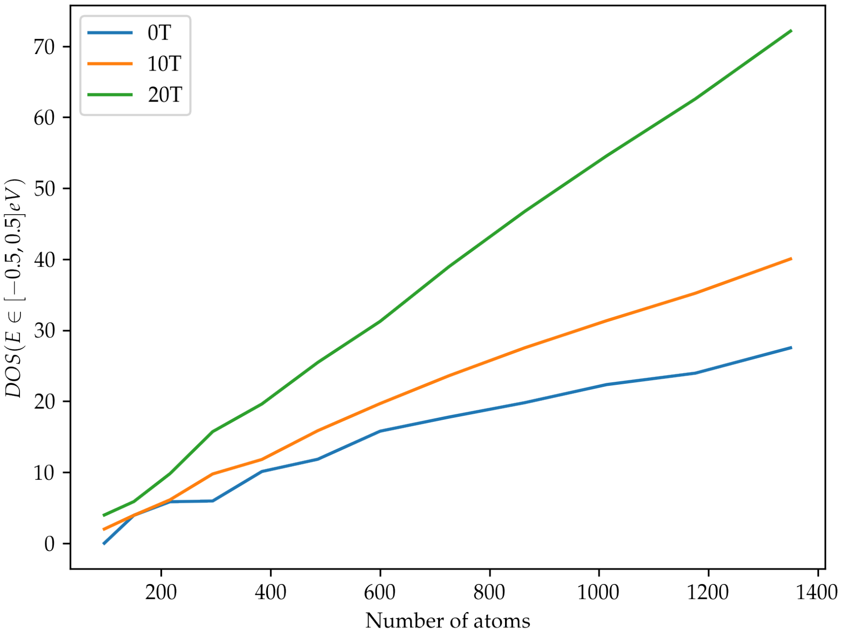

Figure 4.20: Number of states in interval [-0.5,0.5]eV as a function of number of atoms for various uniform magnetic field strengths on an armchair flake. Here, the total DOS is normalized to the total number of orbitals in the lattice.

CHAPTER 5

DISCUSSION AND FUTURE WORK

In this work, we studied the π electronic density of states and local density of states profiles of nanometer-sized graphene structures under magnetic fields using tight-binding method with nearest-neighbor approximation. In order to incorporate a localized magnetic field, we used the so-called optimal gauge2.2.2. We first showed the evolution of the density of states as the structure size increases for various edge shapes4.1. We saw that the edge shapes determined the metallic behavior and while the armchair edges structures start out insulating, they tend towards a semi-metallic state as the structure size increases.

Zigzag edged structures also have an energy gap when the number of atoms is relatively low, and as the size increases, certain localized states emerge near the Fermi level. This characteristic behavior of zigzag edges is studied thoroughly in literature. This localized state does not stem from the bulk structure or the dangling bonds at the edges, rather they are a result of the topology of the π bonds formed at the zigzag edges.

For a mix of armchair and zigzag edges, we studied the Y-shaped junction and this localized state still survived even when the majority of edges were armchair type.

Under the effects of an external magnetic field, both edge types showed very similar behavior, where the magnetic field enhanced the peculiar localized state near the Fermi level. Armchair flakes under a uniform magnetic field showed an interesting behavior where the states localized near the Fermi level were confined to the inner orbitals, leaving the perimeter states almost untouched. We believe that this phenomena needs further exploration.

These localized states showed an increasing trend with both field strength and the width of the field Gaussian function. In the uniform field limit, the total number of states in the emergent peak shows a linear relation with field strength. By looking at the size and field dependence of these localized states, we see that the type of edge plays no role in the enhancement of these states and it is linearly dependent on both the number of atoms enveloped by the Gaussian and the strength of the magnetic field.

This study however does not paint a complete picture. First of all, since we resorted to using an unorthodox gauge, we could not include next-nearest neighbor interactions in this work. Also, although the formulation of this gauge is very simple and straightforward and it gives the correct Aharonov-Bohm phases, it still needs further research to verify its validity, which was out of scope of this thesis.

Last but not least, while the DOS/PDOS profiles give us some idea about the electronic structure of our systems, we also need to study the transport properties of these systems. As such, the study of electronic transport under localized magnetic fields will be the next stage of the author's research.

REFERENCES

[1] J.-W. Rhim and K. Park, "Self-similar occurrence of massless dirac particles in graphene under a magnetic field," *Phys. Rev. B*, vol. 86, p. 235411, Dec 2012.

[2] J. Tersoff, "Energies of fullerenes," *Phys. Rev. B*, vol. 46, pp. 15546–15549, Dec 1992.

[3] C. L. Kane and E. J. Mele, "Size, shape, and low energy electronic structure of carbon nanotubes," *Phys. Rev. Lett.*, vol. 78, pp. 1932–1935, Mar 1997.

[4] Z. Xin, Z. Jianjun, and O.-Y. Zhong-can, "Strain energy and young's modulus of single-wall carbon nanotubes calculated from electronic energy-band theory," *Phys. Rev. B*, vol. 62, pp. 13692–13696, Nov 2000.

[5] J.-C. Charlier, X. Gonze, and J.-P. Michenaud, "Graphite interplanar bonding: Electronic delocalization and van der waals interaction," *Europhysics Letters (EPL)*, vol. 28, pp. 403–408, nov 1994.

[6] P. R. Wallace, "The band theory of graphite," *Phys. Rev.*, vol. 71, pp. 622–634, May 1947.

[7] R. Peierls, "Quelques propriétés typiques des corps solides," *Annales de l'institut Henri Poincaré*, vol. 5, no. 3, pp. 177–222, 1935.

[8] L. LANDAU, "The theory of phase transitions," *Nature*, vol. 138, pp. 840–841, nov 1936.

[9] K. S. Novoselov, A. K. Geim, S. V. Morozov, D. Jiang, Y. Zhang, S. V. Dubonos, I. V. Grigorieva, and A. A. Firsov, "Electric field effect in atomically thin carbon films," *Science*, vol. 306, no. 5696, pp. 666–669, 2004.

[10] E. V. Anslyn and D. A. Dougherty, *Modern physical chemistry*. University Science, 2004.

[11] A. H. Castro Neto, F. Guinea, N. M. R. Peres, K. S. Novoselov, and A. K. Geim, "The electronic properties of graphene," *Rev. Mod. Phys.*, vol. 81, pp. 109–162, Jan 2009.

[12] K. Bolotin, K. Sikes, Z. Jiang, M. Klima, G. Fudenberg, J. Hone, P. Kim, and H. Stormer, "Ultrahigh electron mobility in suspended graphene," *Solid State Communications*, vol. 146, no. 9, pp. 351 – 355, 2008.

[13] D. J. Thouless, M. Kohmoto, M. P. Nightingale, and M. den Nijs, "Quantized hall conductance in a two-dimensional periodic potential," *Phys. Rev. Lett.*, vol. 49, pp. 405–408, Aug 1982.

[14] K. S. Novoselov, A. K. Geim, S. V. Morozov, D. Jiang, M. I. Katsnelson, I. V. Grigorieva, S. V. Dubonos, and A. A. Firsov, "Two-dimensional gas of massless dirac fermions in graphene," *Nature*, vol. 438, pp. 197–200, nov 2005.

[15] K. S. Novoselov, Z. Jiang, Y. Zhang, S. V. Morozov, H. L. Stormer, U. Zeitler, J. C. Maan, G. S. Boebinger, P. Kim, and A. K. Geim, "Room-temperature quantum hall effect in graphene," *Science*, vol. 315, no. 5817, pp. 1379–1379, 2007.

[16] J. Dauber, A. A. Sagade, M. Oellers, K. Watanabe, T. Taniguchi, D. Neumaier, and C. Stampfer, "Ultra-sensitive hall sensors based on graphene encapsulated in hexagonal boron nitride," *Applied Physics Letters*, vol. 106, no. 19, p. 193501, 2015.

[17] A. A. Balandin, S. Ghosh, W. Bao, I. Calizo, D. Teweldebrhan, F. Miao, and C. N. Lau, "Superior thermal conductivity of single-layer graphene," *Nano Letters*, vol. 8, no. 3, pp. 902–907, 2008. PMID: 18284217.

[18] M. I. Katsnelson, "Zitterbewegung, chirality, and minimal conductivity in graphene," *The European Physical Journal B*, vol. 51, pp. 157–160, may 2006.

[19] N. M. R. Peres, A. H. Castro Neto, and F. Guinea, "Conductance quantization in mesoscopic graphene," *Phys. Rev. B*, vol. 73, p. 195411, May 2006.

[20] K. Wakabayashi, M. Fujita, H. Ajiki, and M. Sigrist, "Electronic and magnetic properties of nanographite ribbons," *Phys. Rev. B*, vol. 59, pp. 8271–8282, Mar 1999.

[21] K. Nakada, M. Fujita, G. Dresselhaus, and M. S. Dresselhaus, “Edge state in graphene ribbons: Nanometer size effect and edge shape dependence,” *Phys. Rev. B*, vol. 54, pp. 17954–17961, Dec 1996.

[22] M. Fujita, K. Wakabayashi, K. Nakada, and K. Kusakabe, “Peculiar localized state at zigzag graphite edge,” *Journal of the Physical Society of Japan*, vol. 65, no. 7, pp. 1920–1923, 1996.

[23] K. Wakabayashi, K. ichi Sasaki, T. Nakanishi, and T. Enoki, “Electronic states of graphene nanoribbons and analytical solutions,” *Science and Technology of Advanced Materials*, vol. 11, no. 5, p. 054504, 2010. PMID: 27877361.

[24] Y.-W. Son, M. L. Cohen, and S. G. Louie, “Energy gaps in graphene nanoribbons,” *Phys. Rev. Lett.*, vol. 97, p. 216803, Nov 2006.

[25] K. Wakabayashi, “Electronic transport properties of nanographite ribbon junctions,” *Phys. Rev. B*, vol. 64, p. 125428, Sep 2001.

[26] K. Wakabayashi and M. Sigrist, “Zero-conductance resonances due to flux states in nanographite ribbon junctions,” *Phys. Rev. Lett.*, vol. 84, pp. 3390–3393, Apr 2000.

[27] H. P. Heiskanen, M. Manninen, and J. Akola, “Electronic structure of triangular, hexagonal and round graphene flakes near the fermi level,” *New Journal of Physics*, vol. 10, p. 103015, oct 2008.

[28] J. C. Slater and G. F. Koster, “Simplified lcao method for the periodic potential problem,” *Phys. Rev.*, vol. 94, pp. 1498–1524, Jun 1954.

[29] F. Bloch, “Über die quantenmechanik der elektronen in kristallgittern,” *Zeitschrift für Physik*, vol. 52, pp. 555–600, Jul 1929.

[30] R. M. Martin, *Electronic structure: basic theory and practical methods*. Cambridge University Press, 2013.

[31] Y. Hancock, A. Uppstu, K. Saloriutta, A. Harju, and M. J. Puska, “Generalized tight-binding transport model for graphene nanoribbon-based systems,” *Phys. Rev. B*, vol. 81, p. 245402, Jun 2010.

[32] W. A. Harrison, *Electronic structure and the properties of solids: the physics of the chemical bond.* Dover Publications, 1989.

[33] R. Peierls, "Zur theorie des diamagnetismus von leitungselektronen," *Zeitschrift für Physik*, vol. 80, pp. 763–791, Nov 1933.

[34] Y. Aharonov and D. Bohm, "Significance of electromagnetic potentials in the quantum theory," *Phys. Rev.*, vol. 115, pp. 485–491, Aug 1959.

[35] D. R. Hofstadter, "Energy levels and wave functions of bloch electrons in rational and irrational magnetic telds," *Phys. Rev. B*, vol. 14, pp. 2239–2249, 09 1976.

[36] G. Metalidis, *Electronic Transport in Mesoscopic Systems.* CreateSpace Independent Publishing Platform, 2015.

[37] M. Inui, S. A. Trugman, and E. Abrahams, "Unusual properties of midband states in systems with off-diagonal disorder," *Phys. Rev. B*, vol. 49, pp. 3190–3196, Feb 1994.

[38] D. L. Miller, K. D. Kubista, G. M. Rutter, M. Ruan, W. A. de Heer, P. N. First, and J. A. Stroscio, "Observing the quantization of zero mass carriers in graphene," *Science*, vol. 324, no. 5929, pp. 924–927, 2009.

[39] P. G. Harper, "The general motion of conduction electrons in a uniform magnetic field, with application to the diamagnetism of metals," *Proceedings of the Physical Society. Section A*, vol. 68, pp. 879–892, oct 1955.

APPENDIX A

PEIERLS SUBSTITUTION

In the presence of a magnetic field, the Hamiltonian is given by

$$\widetilde{H} = \frac{(\mathbf{p} - q\mathbf{A})^2}{2m} + U(\mathbf{r}) \tag{A.1}$$

and due to the additional term, the wavefunction for the particle picks up an additional factor

$$|\widetilde{\psi}\rangle = |\psi\rangle e^{i\frac{q}{\hbar}\int\limits_{\mathbf{R}}^{\mathbf{r}} \mathbf{A}(\mathbf{r}').\mathbf{dr}'} \tag{A.2}$$

where $\mathbf{A}$ is a vector potential for a given field. In the tight-binding method, let us consider changing the Bloch sums to reflect this

$$\begin{aligned}\widetilde{\varphi}(\mathbf{r}) &= \frac{1}{\sqrt{N}} \sum_{\mathbf{R}} e^{i\mathbf{k}.\mathbf{R}} e^{i\frac{q}{\hbar}\int\limits_{\mathbf{R}}^{\mathbf{r}} \mathbf{A}(\mathbf{r}').\mathbf{dr}'} \phi_{\mathbf{R}}(\mathbf{r} - \mathbf{R}) \\ &= \frac{1}{\sqrt{N}} \sum_{\mathbf{R}} e^{i\mathbf{k}.\mathbf{R}} \widetilde{\phi}_{\mathbf{R}}(\mathbf{r} - \mathbf{R})\end{aligned} \tag{A.3}$$

We can show that $\widetilde{\phi}$ are the new eigenstates of the Hamiltonian A.1 with the same eigenvalues as the zero-field case. With $U(\mathbf{r}) = 0$ for simplicity and $\mathbf{p} = -i\hbar\nabla$, we have

$$\begin{aligned}\widetilde{H}\widetilde{\phi}(\mathbf{r}) &= e^{i\mathbf{k}.\mathbf{R}} \Big[\frac{(-i\hbar\nabla - q\mathbf{A})^2}{2m}\Big] e^{i\frac{q}{\hbar}\int_{\mathbf{R}}^{\mathbf{r}} \mathbf{A}(\mathbf{r}').\mathbf{dr}'} \phi_{\mathbf{R}}(\mathbf{r} - \mathbf{R}) \\ &= e^{i\mathbf{k}.\mathbf{R}} \Big[\frac{(-\hbar^2\nabla^2 - i\hbar q\nabla.\mathbf{A} + q^2\mathbf{A}^2)}{2m}\Big] e^{i\frac{q}{\hbar}\int_{\mathbf{R}}^{\mathbf{r}} \mathbf{A}(\mathbf{r}').\mathbf{dr}'} \phi_{\mathbf{R}}(\mathbf{r} - \mathbf{R}) \\ &= e^{i\mathbf{k}.\mathbf{R}} \Big[\frac{(-\hbar^2\nabla^2 - i - q^2\mathbf{A}^2 + q^2\mathbf{A}^2)}{2m}\Big] e^{i\frac{q}{\hbar}\int_{\mathbf{R}}^{\mathbf{r}} \mathbf{A}(\mathbf{r}').\mathbf{dr}'} \phi_{\mathbf{R}}(\mathbf{r} - \mathbf{R}) \\ &= e^{i\mathbf{k}.\mathbf{R}} e^{i\frac{q}{\hbar}\int_{\mathbf{R}}^{\mathbf{r}} \mathbf{A}(\mathbf{r}').\mathbf{dr}'} \hat{H}\phi_{\mathbf{R}}(\mathbf{r} - \mathbf{R})\end{aligned} \tag{A.4}$$

where going from the second to the third line, we assumed that the vector potential varies slowly over the lattice scale so that $\nabla.\mathbf{A} = 0$. We see that with the given approximation, the problem is just reduced to dealing with the extra phase factors coming from the basis functions. Using A.4, we can express the modified hopping parameters $\widetilde{t}$ between lattice sites $\mathbf{R}$ and $\mathbf{R}'$ in Dirac notation

$$\begin{aligned}\widetilde{t}_{\mathbf{R}\mathbf{R}'} &= \langle \widetilde{\phi}_{\mathbf{R}'} | \widetilde{H} | \widetilde{\phi}_{\mathbf{R}} \rangle \\ &= \langle \phi_{\mathbf{R}'} | e^{-i\frac{q}{\hbar}\int\limits_{\mathbf{R}'}^{\mathbf{r}} \mathbf{A}(\mathbf{r}').\mathbf{dr}'} H e^{i\frac{q}{\hbar}\int\limits_{\mathbf{R}}^{\mathbf{r}} \mathbf{A}(\mathbf{r}').\mathbf{dr}'} | \phi_{\mathbf{R}} \rangle \\ &= e^{i\frac{q}{\hbar}\int\limits_{\mathbf{R}}^{\mathbf{R}'} \mathbf{A}(\mathbf{r}').\mathbf{dr}'} \langle \phi_{\mathbf{R}'} | e^{i\frac{q}{\hbar}\Phi_{\mathbf{R},\mathbf{r},\mathbf{R}'}} H | \phi_{\mathbf{R}} \rangle\end{aligned} \tag{A.5}$$

where $\Phi_{\mathbf{R},\mathbf{r},\mathbf{R}'}$ is the closed loop line integral of $\mathbf{A}$ along the three points and going to the last line we have used the fact that

$$\int_{\mathbf{R}}^{\mathbf{r}} \mathbf{A}(\mathbf{r}').\mathbf{dr}' + \int_{\mathbf{r}}^{\mathbf{R}'} \mathbf{A}(\mathbf{r}').\mathbf{dr}' = \Phi_{\mathbf{R},\mathbf{r},\mathbf{R}'} - \int_{\mathbf{R}'}^{\mathbf{R}} \mathbf{A}(\mathbf{r}').\mathbf{dr}' \tag{A.6}$$

We can show that the flux term $\Phi_{\mathbf{R},\mathbf{r},\mathbf{R}'}$ is negligibly small by two observations. When $\mathbf{r}$ is far away from the lattice points $\mathbf{R}$ and $\mathbf{R}'$, the flux is large but since the atomic orbitals are highly localized at these two lattice points, the value of the hopping term is very small and the whole hopping term goes to zero. When $\mathbf{r}$ is at or near any of these lattice points, the triangle formed is small, and assuming small B-fields, the flux term $\Phi_{\mathbf{R},\mathbf{r},\mathbf{R}'}$ goes to zero, giving us the modified hopping parameters as

$$\widetilde{t}_{\mathbf{R}\mathbf{R}'} \approx t_{\mathbf{R}\mathbf{R}'} e^{i\frac{q}{\hbar}\int\limits_{\mathbf{R}}^{\mathbf{R}'} \mathbf{A}(\mathbf{r}').\mathbf{dr}'} \tag{A.7}$$

APPENDIX B

HARPER'S EQUATION

Let us consider the case of a square lattice with a single atom basis under a uniform magnetic field given by the Landau gauge $\mathbf{A} = (0, Bx, 0)$2.2.1. Substituting the proper hopping parameters when a magnetic field is present, the Hamiltonian is given as

$$H = t\big[e^{ik_xa} + e^{-ik_xa} + e^{ik_ya}e^{i2\pi\frac{Bx}{\Phi_0}} + e^{-ik_ya}e^{-i2\pi\frac{Bx}{\Phi_0}}\big] \tag{B.1}$$

We established in 2.2 that when translated by a lattice vector $\mathbf{R}$, the wavefunction for an electron in a periodic lattice picks up a phase accordingly. This lets us define $\varphi(x + a, y) = e^{ik_xa}\varphi(x, y)$ and $\varphi(x, y + a) = e^{ik_ya}$. Substituting $x = ma$ and $y = na$ for the given square lattice, we can express the time-independent Schrödinger equation as

$$t\Bigg[\varphi(m{+}1, n){+}\varphi(m{-}1, n){+}e^{i2\pi\frac{Bxa}{\Phi_0}}\varphi(m, n{+}1){+}e^{-i2\pi\frac{Bxa}{\Phi_0}}\varphi(m, n{-}1)\Bigg] = E\varphi(m, n) \tag{B.2}$$

Since the phase factors are independent of the coordinate y, we can assume the partial solution for y to be in the form $\chi(y) = e^{ik_yna}$, which reduces B.2 to

$$t[\varphi(m{+}1){+}\varphi(m{-}1){+}e^{i2\pi\frac{Ba^2m}{\Phi_0}}e^{ik_ya}\varphi(m){+}e^{-i2\pi\frac{Ba^2m}{\Phi_0}}e^{-ik_ya}\varphi(m)] = E\varphi(m) \tag{B.3}$$

and we have

$$\varphi(m - 1) + \varphi(m + 1) + 2\varphi(m)cos(2\pi m\Phi/\Phi_0 - k_ya) = \epsilon\varphi(m) \tag{B.4}$$

where $\epsilon \equiv E/t$ is the energy in units of t and $\Phi = Ba^2$ is the magnetix flux piercing the unit cell. This is called the Harper's equation[39]. Since different m values give different equations, one reaches a unique set of equations when Φ/Φ_0 is a rational number p/q and m goes through q different values, essentially resulting in the Hamiltonian matrix written for a magnetic unit cell enlarged in x direction q times2.2.1